**STUDY OF THE $\Xi_b^-$ BARYON DECAY AT CMS**

By

Sandra Nathaly Santiesteban

A thesis submitted in partial fulfillment of the requirements for the degree of

MASTER OF SCIENCE

in

PHYSICS

UNIVERSITY OF PUERTO RICO
MAYAGÜEZ CAMPUS

2014

Approved by:

| | |
|---|---|
| Juan Eduardo Ramírez-Vargas, Ph.D.<br>President, Graduate Committee | Date |
| Samuel A. Santana-Colón, Ph.D.<br>Member, Graduate Committee | Date |
| Héctor Méndez-Mella, Ph.D.<br>Member, Graduate Committee | Date |
| Juan A. Ortíz, Ph.D.<br>Representative of Graduate Studies | Date |
| Rafael A. Ramos, Ph.D.<br>Chairperson of the Department | Date |

Abstract of Dissertation Presented to the Graduate School
of the University of Puerto Rico in Partial Fulfillment of the
Requirements for the Degree of Master of Science

**STUDY OF THE $\Xi_b^-$ BARYON DECAY AT CMS**

By

Sandra Nathaly Santiesteban

2014

Chair: Juan Eduardo Ramírez Vargas
Major Department: Physics

A preliminary measurement of the $\Xi_b^-$ baryon lifetime through the decay chain $\Xi_b^- \rightarrow J/\psi\Xi^-$, where $J/\psi \rightarrow \mu^+\mu^-$, $\Xi^- \rightarrow \Lambda^0\pi^-$ and $\Lambda^0 \rightarrow p\pi^-$, using 5.1 $fb^{-1}$ of integrated luminosity of data from proton-proton collisions with a center-of-mass energy of 7 $TeV$ collected by the Compact Muon Solenoid CMS at CERN is presented.

After the reconstruction and selection of the $\Xi_b^-$ baryon from the data, 65 candidates with a mass of $5.798 \pm 0.015\ GeV/c^2$ were found. Then, the reduced proper time of the $\Xi_b^-$ candidates were calculated in order to use the binned maximum likelihood method to measure the lifetime of the particle.

Finally, the preliminary lifetime $\tau = 1.597 \pm^{0.293}_{0.262} \pm 0.060\ ps$ was measured, where the first error is statistical and the second is systematic.

Resumen de Disertación Presentado a Escuela Graduada
de la Universidad de Puerto Rico como requisito parcial de los
Requerimientos para el grado de Maestría en Ciencias

**ESTUDIO DEL DECAIMIENTO DEL BARION $\Xi_b^-$ EN EL CMS**

Por

Sandra Nathaly Santiesteban

2014

Consejero: Juan Eduardo Ramírez Vargas
Departamento: Física

Esta tesis presenta una medida preliminar del tiempo de vida del barión $\Xi_b^-$ a través del canal de decaimiento $\Xi_b^- \to J/\psi\Xi^-$, donde $J/\psi \to \mu^+\mu^-$, $\Xi^- \to \Lambda^0\pi^-$ y $\Lambda^0 \to p\pi^-$, con 5.1 $fb^{-1}$ de luminosidad integrada y centro de masa de 7 $TeV$, de datos provenientes de colisiones protón-protón en el Solenoide Compacto de Muones CMS en CERN.

Después de la reconstrucción y selección de los bariones $\Xi_b^-$ de la muestra de datos, se encontraron 65 candidatos con una masa de $5.798 \pm 0.015\ GeV/c^2$. Posteriormente, se calculó el tiempo propio reducido de los candidatos a $\Xi_b^-$ con el fin de utilizar el método de máxima probabilidad para medir el tiempo de vida de la partícula.

Finalmente, el tiempo de vida preliminar $\tau = 1.597 \pm^{0.293}_{0.262} \pm 0.060\ ps$ fue medido, en donde el primer error es estadístico y el segundo es sistemático.

To god

To my beloved family:

Every step in my way is possible because my two moms Luciana and Maria, and my almost sister Marisol have always been there for me.

In some point in my life I found a big support. To my loved Juan who have always encouraged me.

The light of my life, my little Sara. To her are and will be all my achievements.

ACKNOWLEDGMENTS

A research is never the work of anyone alone. The contributions of many different people, in their different ways, have made this possible. I would like to express my gratitude especially to the following.

First of all, I am deeply grateful to my advisor Dr. Juan Eduardo Ramíre, for his support, patience and guidance throughout my master studies. He and the HEP group, to let me work in this amazing project as CMS represent. Specially, in the HEP group to Dr. Angel Lopez and Dr. Héctor Méndez for their support. To work with you has been a real pleasure to me, with heaps of fun and excitement.

My thanks also go to the professors of the RUM for their guidance. In special, to Dr. Erick Roura, Dr. Héctor Jiménez, Dr. Samuel Santana and Dr. Roberto Lopez who were highly helpful and offered invaluable assistance and support.

I would like to thank to my best friends Juan Ito and Sindy. You have been there always listened and encouraged me.

Also, to my friends in Colombia, Luz, Lorena, Diana, Fredy, Zonia, Nico, Gerrman, between others. I would like to thank you for support me and my family while I was far.

And last but not least to my new friends, Ms. Teresita Gaud who adopted me in her house and give me the sweetness of home. Maria Andrea, Jeremiah, Daniel and Amanda who have help me and are great friends. At the University, to Indira, Sergio, Mi combo Peruano, Soraya, Carlos, Omar, Waleska, Vanesa, Ronal and his family, and more, who have been there. Thank you so much, I will take you in my memory.

I am going to miss Puerto Rico. This place is beautiful and its people is realy kind.

TABLE OF CONTENTS

LIST OF TABLES

LIST OF FIGURES

# CHAPTER 1
# THEORETICAL AND EXPERIMENTAL OVERVIEW

The elementary particles are recognized as those whose structure cannot be described as a composition of smaller particles. To understand the interactions between the elementary particles and their characteristics, a better understanding of the Universe is needed. The understanding of elementary particles requires answering questions such as, "What is the universe made of?", "What is matter and what holds it together?", among others. Many theories and discoveries have been developed since ancient times in order to find the type of elements that build all the matter. However, as time passes, more surprises reveal a lack of understanding about the universe. As a consequence today, the scientific community works harder to find smaller structures and theories in large experiments around the world.

Between the years 1970 to 1973, a theory known as the Standard Model (SM) was developed [1]. Currently, the SM is the best description of the building blocks of matter, and how they interact. This chapter describes important features and the structure of the SM and the experiments to detect fundamental particles, especially the *Large Hadron Collider* (LHC).

## 1.1 Elementary Particles

The SM is composed of fermions, which make up matter and antimatter, and bosons, which are the force-carrier particles. The fermions are particles with half-integer spin and characterized by the Pauli exclusion principle (no two identical fermions may occupy the same quantum state simultaneously), and the bosons are particles with integer spin (two or more bosons can occupy the same quantum state simultaneously) [2]. Additionally,

each particle in the SM has its corresponding antiparticle which has the same properties of the particle but opposite charge.

### 1.1.1 Fermions: The elementary particles of matter

The elementary particles that belong to the fermions group are quarks and leptons, which are classified into three generations. The quarks are particles of fractional electrical charge of the electron charge magnitude ($e = 1.6 \times 10^{-19}\ C$), and the leptons may have integer or no charge.

There are six types of quarks in the three generations called "up" ($u$) and "down" ($d$) in the first generation, "charm" ($c$) and "strange" ($s$) in the second generation, and "top" ($t$) and "bottom" or "beauty" ($b$) in the third generation. The characteristics of the quarks are shown in Figure 1–1. Quarks have not been detected as free particles, they exist in bound called "Hadrons". For instance, the internal structure of particles, such as the neutron and the proton, is given by the combination of quarks [2].

There are six particles in the leptons group: "electron" ($e$) and "electron neutrino" ($\upsilon_e$) in the first generation, "muon" ($\mu$) and " muon neutrino" ($\upsilon_\mu$) in the second generation, and "tau" ($\tau$) and "tau neutrino" ($\upsilon_\tau$) in the third generation. The $e$, $\mu$ and $\tau$ leptons have an electric charge corresponding to $-1$ of the electron charge magnitude, whereas the neutrinos have no charge (see Figure 1–1). Additionally, the neutrinos mass do not have an exact value in the SM; however, there is evidence that neutrinos have mass and limits on the value of these masses have been imposed at the experiments. As a consequence of being electrically neutral and being of little mass, the neutrinos interact rarely with matter [4]. The mistery of neutrino mass is studied by theories beyond of the SM.

Finally, fermions interact through four fundamental forces which use bosons as intermediate particles.

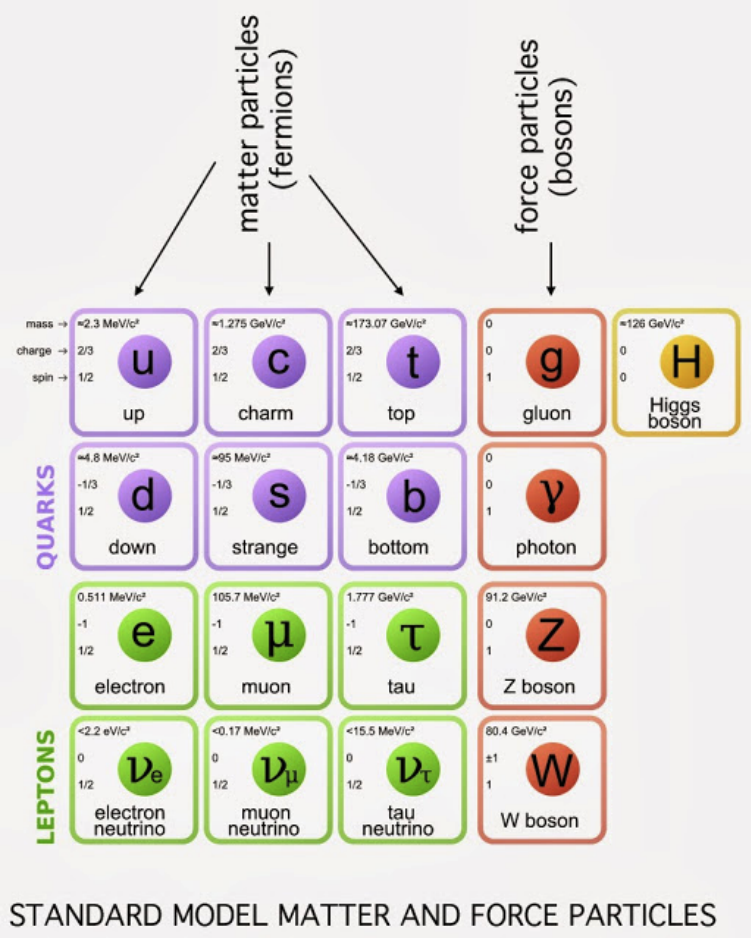


Figure 1–1: Fermions and bosons.
(Taken from [3]).

### 1.1.2 Bosons: Force-carrier particles

There are four fundamental interactions that affect fermions: i) weak, ii) strong, iii) electromagnetic, and iv) gravitational, which use mediating particles called "bosons" [5] (See Figure 1–2). However, even though the gravitational force is a fundamental interaction, it is not explained by the SM. The electromagnetic and gravitational forces have unlimited range, while the weak and strong forces have influence at very short distances no greater than the atomic nucleus radius. Some of the main features of the fundamental interactions are described below.

- **Weak Interaction**. The weak force is related with the emission or absorption of $W^{\pm}$ and $Z$ bosons, which have spin 1 and are more massive than the proton and electron. The characteristics of the $W^{\pm}$ (almost 80 times as massive as the proton) and the $Z$ (almost 90 times as massive as the proton) bosons are shown in the Figure 1–1 [6]. The weak interaction acts in quarks and leptons. For example, the Figure 1–2 shows a beta decay, where one neutron decayed into one proton, one electron and one electron antineutrino since one $d$ quark in the neutron decayed into one $u$ quark which forms one proton while one $\bar{\upsilon_e}$ and one $e$ scapes of the hadron.

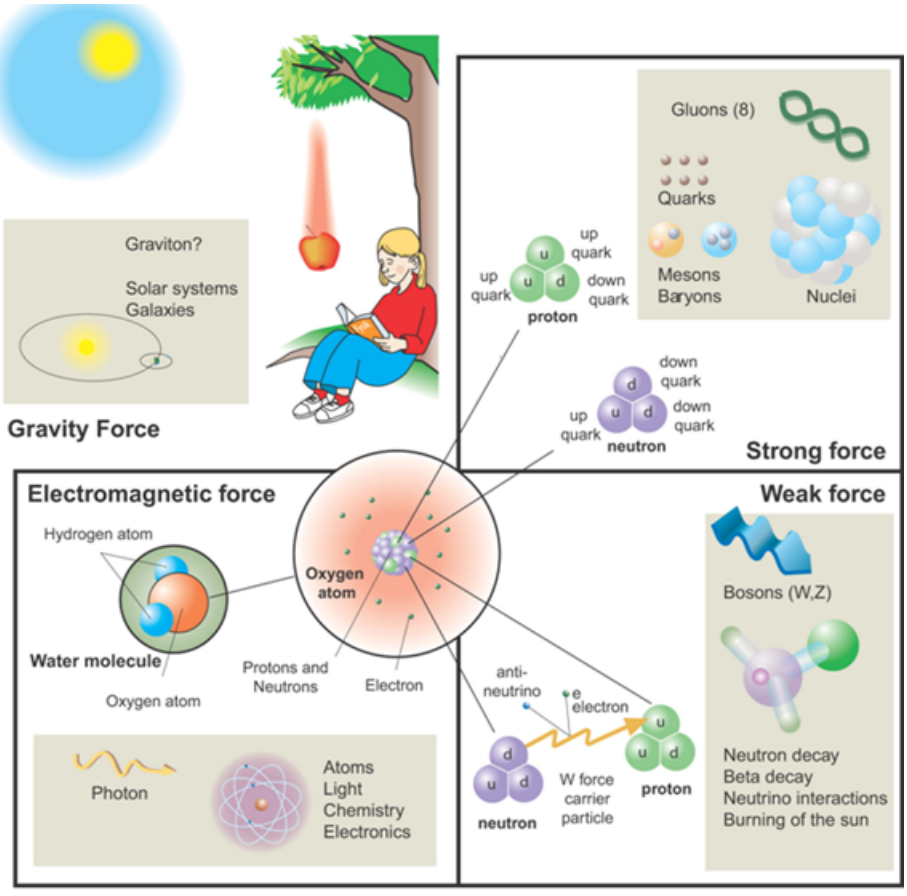


Figure 1–2: The four fundamental interactions. (Taken from [7]).

- **Strong Interaction**. The strong force is mediated by the "gluon" ($g$), a massless particle of spin 1 (See Figure 1–1). A quark is joined to one or two others quarks by gluons forming hadrons where the gluon acts as a glue. When the quarks which make up a hadron are close, they have a kind of free movement; however, when the distance between quarks increases, the force between the quarks increase too; this is known as *asymptotic freedom* [6]. Therefore as is shown in Figure 1–2, the strong force holds the nucleus together and is responsible for the stability of matter. The force has a range of $10^{-13}$ $cm$, and is the strongest of the four interactions. This interaction is also known as the color force because of Quarks and gluons have a property called color charge. There are three types of color charges (red, green, and blue) and their corresponding anticolor charges, and the Quarks constantly change their color charge as they exchange gluons with other quarks.
- **Electromagnetic Interaction**. This interaction [6] can be a repulsive or an attractive force, and it acts on charged particles. Thus the electromagnetic interaction is responsible for binding fermions into atoms and atoms into molecules (see Figure 1–2). The mediated particle is the *photon* ($\gamma$), which is massless and has spin 1 (See Figure 1–1).
- **Gravitational Interaction**. This force acts on all particles with mass and is the weakest of the four interactions although it has an unlimited range. Therefore, for small particles like quarks and fermions it is practically negligible [6]. However, in a macroscopic scale, this force describes the dynamics of falling bodies, planets, stars, among others. Nevertheless, the SM can not describe the gravity interaction. Some theories predict that the mediating particle in the gravitational interaction is the *graviton*, a massless boson of spin 2, which has not been found yet.

To summarize, there are four fundamental forces in the universe and each one of them does not act on all particles. In addition, the SM is the best description of the universe, but it does not describe the gravitational force or the neutrino masses.

### 1.1.3 Higgs Boson

In addition to the particles and interactions described in the two previous subsections, it is necessary to explain how these particles acquire mass. All the elementary particles acquire mass through their interaction with the *Higgs Field*. This mechanism is called the *Higgs Mechanism*.

The SM does not directly predict the values of the Higgs boson mass (See Figure 1–1) and therefore many ranges of energy were studied. Finally, the *Higgs Boson* discovery was announced at the European Organization for Nuclear Research (CERN) on July 4, 2012. They published a mass estimate of 125.3± 0.4 ($stat.$) ±0.5 ($syst.$) $GeV$ [8]. The other properties and characteristics of the Higgs are still being studied.

## 1.2 Hadrons and the $\Xi_b^-$ baryon

A hadron is any particle that is made from quarks, antiquarks and gluons, because of, quarks and antiquarks are bound into composite particles by the strong interaction. In the universe, there exists a great number of hadrons which are divided in two principal groups, i) Mesons and ii) Baryons.

Some properties of the hadrons are given by the baryon number, strangeness, charmness, upness, bottomness, downness, topness, and their electric charge. For example, the hadron charge is the sum of the quarks charges inside; the quarks charge is fractionary and the hadron charge is integer. Moreover, the hadrons are particles which experience the weak and strong interaction, and the charged ones, electromagnetic interactions [5]. In this thesis, the $\Xi_b^-$ particle will be studied; this particle is a baryon. The principal characteristics of the hadrons and specially the particles related with the $\Xi_b^-$ decay are explained below.

### 1.2.1 Mesons

A meson is a hadron made of one quark and one antiquark. In general, mesons have a radius of the order of the femtometre ($10^{-15}m$) and are unstable particles which decay quickly. In the Big Bang massive mesons were created, despite this they are rarely found in nature today; however, they are created in high energy experiments and are used to understand the composition of the Universe.

Mesons are bosons due to quarks having spin 1/2 and the spin sum in a meson is 1 (or 0 in some cases), each meson has its corresponding antiparticle (antimeson) in which the quarks are replaced by their corresponding antiquarks. The mesons have weak and strong interactions, furthermore, charged mesons also participate in the electromagnetic interaction [5]. Table 1–1 shows some properties of the two mesons involved in the $\Xi_b^-$ decay. The masses are given by the average published by the Particle Data Group (PDG) [9].

Table 1–1: List of Mesons involved in the $\Xi_b^-$ decay

| Meson | Quarks Content | Rest mass($MeV/c^2$) | Charge ($e$) |
|---|---|---|---|
| $J/\psi$ | $c\bar{c}$ | $3096.916 \pm 0.011$ | 0 |
| $\pi^-$ | $d\bar{u}$ | $139.57018 \pm 0.00035$ | $-1$ |

### 1.2.2 Baryons

A baryon is composed of three quarks, and its antiparticle (antibaryon) is composed by the corresponding three antiquarks. The baryon is a fermion since its spin is the sum of the spin of its quarks which gives 3/2 or 1/2. Also, baryons can be charged or not charged particles [5].

The most known baryons are the proton and the neutron which compose atoms. The proton is made of the $u$, $u$ and $d$ quarks, and the neutron is made of $u$, $d$ and $d$ quarks; furthermore, both have spin 1/2. In general, the other baryons (even the neutron when is isolated) are unstable and they decay into more lightly particles. In this thesis,

the baryon $\Xi_b^-$ will be studied and the baryons involved in its decay are in the Table 1–2, the masses are given by the average published by the Particle Data Group (PDG) [9].

Table 1–2: List of Baryons involved in the $\Xi_b^-$ decay

| Meson | Quarks Content | Rest mass($MeV/c^2$) | Charge ($e$) |
|---|---|---|---|
| $\Xi^-$ | $dss$ | $1321.71 \pm 0.07$ | $-1$ |
| $\Lambda^0$ | $uds$ | $1115.683 \pm 0.006$ | 0 |

### 1.2.3 The $\Xi_b^-$ baryon

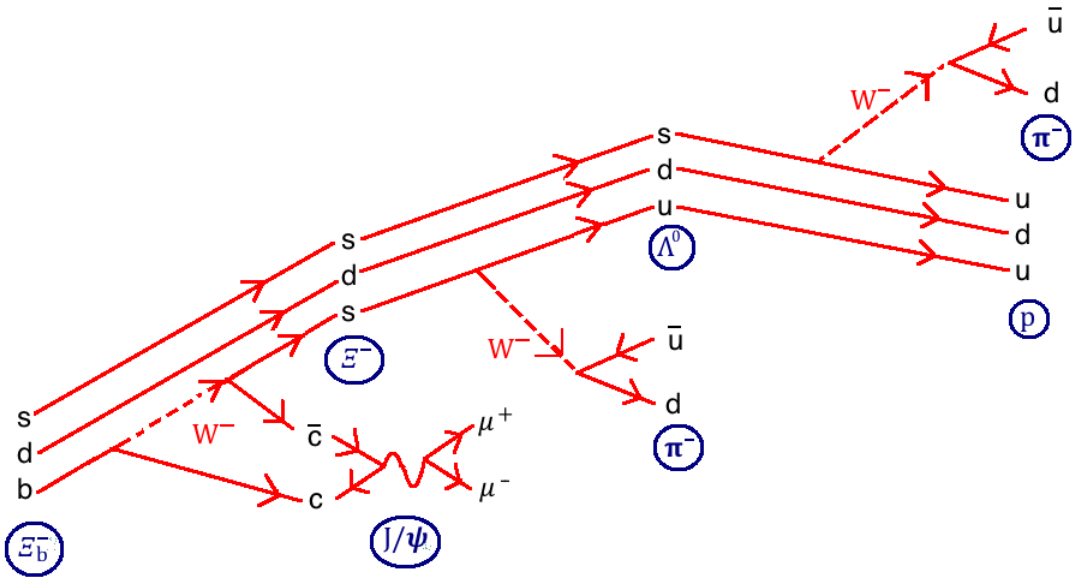


Figure 1–3: $\Xi_b^-$ decay topology.

The $\Xi_b^-$ baryon is composed of $d$, $s$ and $b$ quarks. In this thesis the topology studied is $\Xi_b^- \to J/\psi\Xi^-$ with $J/\psi \to \mu^+\mu^-$, $\Xi^- \to \Lambda^0\pi^-$ and $\Lambda^0 \to p\pi^-$; where the $\Xi_b^-$, $\Xi^-$ and $\Lambda^0$ decays are due to weak interactions. The topology of this decay is shown in Fig 1–3.

The $\Xi_b^-$ particle was discovered by $D\emptyset$ and CDF experiments at Fermilab. The discovery was announced on 12 June 2007 [10]. Its charge corresponds to $-e$ and its mass is $5791.1 \pm 2.2\ MeV/c^2$. Also, according with the PDG [9], its lifetime is $1.56 \pm^{0.27}_{0.25} \pm 0.02$ $(ps)$. Finally, an interesting remark of this baryon refers to its quark content which is from all three quark generations.

### 1.3 Beyond the Standard Model

The SM of particle physics is the best description of fundamental particles because it is a mathematically consistent theory and it is compatible with nearly all experimental results. However, there still remain open questions like, "Why are there three families of quarks and leptons?", "Why is the electric charge quantized?". "What is the origin of quark and lepton mixings?", "What is the origin of matter-antimatter asymmetry?" "What is the role of gravity?", among others. Consequently, some theories [11] have emerged to try to solve all these questions and explain how the Universe works. Below a brief description of these new theories.

- *Grand Unified Theories (GUT)*: unify the three gauge interactions of the Standard Model which define the electromagnetic, weak, and strong interactions into one single interaction characterized by one larger gauge symmetry and thus one unified coupling constant.
- *Supersymmetry (SUSY)*: predict the existence of supersymmetric particles (*sparticles*) which include the *sleptons*, *squarks*, *neutralinos* and *charginos*. Each particle in the SM has a superpartner called Superparticle. Among their principal features, superparticles are heavier and can not be easy produce by current colliders.
- *String Theory*: in this theory all the elementary particles arise from the different quantum states of the *strings*, which describes the motion of a particle by drawing a graph of its position with respect to time. Furthermore, this theory includes the gravitational

interaction with the other three interactions and requires the existence of more dimensions (besides the one of time and three spacial known); it is expected that the other dimensions be compressed.

## 1.4 Detection of Elementary Particles

To study and to obtain more information about the structure of matter, scientists have developed accelerators. In accelerators, particles are accelerated using electromagnetic fields and may collide with other beam of particles or with a fixed target. Around of the collision point are the detectors which use different technologies to detect the particles.

The beam of particles used in accelerators is made of electrons, protons, positrons or ions. Usually, to obtain these particles the procedure is as follows:

- The electrons are emitted from a heated filament and are moved using electric and magnetic fields.
- Photon beams of high energy (obtained of a prior bombardment of a material with high energy electrons) collide against a target in order to obtain electrons and positrons . The separation of these particles is done by electromagnetic fields.

In addition, the different accelerators can be classified in *Linacs*, *Cyclotrons* and *Synchrotrons* [12].

- *Linacs.* These are based on the use of a varying electric field to increase the voltage. Initially, the particles are passed through a system of metal tubes in a straight line, which are located to prevent that the particles can feel the others particles field when they go in opposite direction. The tubes used have lengths that increase in correspondence with the increasing rate of the accelerated particles. Thus, the principal disadvantage is that, because the particles travel in a straight line, each accelerating

segment is used only once. Then, in order to achieve particle beams with even higher energy, it is necessary to add segments to the length of the *Linac*.

- *Cyclotrons*. In these accelerators, the charged particles are accelerated outwards from the center along a spiral path. These are based on bending the trajectories of particles using magnets. The particles are accelerated several times and are synchronized to the same phase of the electric field. The particles are accelerated when they pass between two semicircular electrodes ("D" shaped electrodes) subjected to an alternating voltage. However, as the speed of the particles approaches that of light, then, the relativistic mass increase becomes significant and this results in the charges arriving too late to be accelerated across the gap between two "D" shaped electrodes.
- *Synchrotrons*. These accelerators have a storage ring which vary the magnetic field strength in time, then the particles move in a circular path and to obtain greater energies the fields increase. *Synchrotrons* allowed a big jump in terms of obtaining higher energies. In other words, *Synchrotrons* have an increasing magnetic field which confines a beam of accelerated charged particles to an orbit of fixed radius. Furthermore, *Synchrotrons* are very large and very expensive machines but they are capable of much higher energies than cyclotrons. The first synchrotron used was the Cosmotron in the Brookhaven National Laboratory (New York), and began operations in 1952, achieving an energy of 3 $GeV$.

### 1.4.1 The Large Hadron Collider (LHC)

Currently, the Large Hadron Collider (LHC) at the European Organization for Nuclear Research (CERN) beneath the Franco-Swiss border near Geneva, Switzerland is the world's biggest and most powerful particle accelerator.

The LHC is installed in a tunnel with a circumference of 27 $km$ and 175 $m$ beneath the Franco-Swiss border. It was designed for a centre-of-mass energy up to 14 TeV and a luminosity of $10^{34} cm^{-2} s^{-1}$; however, the center of mass energy was 7 $TeV$ in 2011 and

8 $TeV$ in 2012 (this terms will be explained later) [13]. Almost 10,000 scientists and engineers from different countries around the world work in this accelerator.

Particles sources an pre-accelerators are used to prepare the beams for the LHC (see Figure 1–4). The source of protons is a bottle of hydrogen gas where an electric field is used to strip hydrogen atoms of their electrons to yield protons. After, the protons are accelerated with a Linear Accelerator (Linac 2) to 50 $MeV$ of energy. Then, the beam is injected to the Proton Synchrotron Booster (PSB) which accelerates the protons to 1.4 $GeV$ followed by the Proton Synchrotron (PS), pushing the beam to 25 $GeV$. Protons are then sent to the Super Proton Synchrotron (SPS) where they are accelerated to 450 $GeV$. Finally, the protons are transferred to the two beam pipes of the LHC [13].

If the source is ions then, they are obtained from vaporized lead and enter to the Linac 3 before being collected and accelerated in the Low Energy Ion Ring (LEIR). Afterwards, they follow the same route to get the maximum energy as the protons in the LHC.

Furthermore, LHC has two beams which collide at four different points and used diople magnets to deflect the beams in circular paths while many quadrupole magnets keep the beams focused. Additionally, liquid helium is used to keep magnets at 1.9 $K$ which is their operating temperature, since they need to be kept at colder temperatures to obtain zero electrical resistance (Superconductivity).

LHC was built to answer the biggest questions about the Universe and how it works. Consequently, to show evidence of SUSY, extra dimensions, Dark Matter and Dark Energy or give some clues about the Grand Unified Theory. The biggest discovery of the LHC so far is the "*Higgs Bosson*".

In the LHC ring [13] are seven experiments:

- The biggest are the ***Toroidal LHC Apparatus*** (ATLAS) and the ***Compact Muon Solenoid*** (CMS). They are general purpose detectors designed for the *Higgs Bosson*

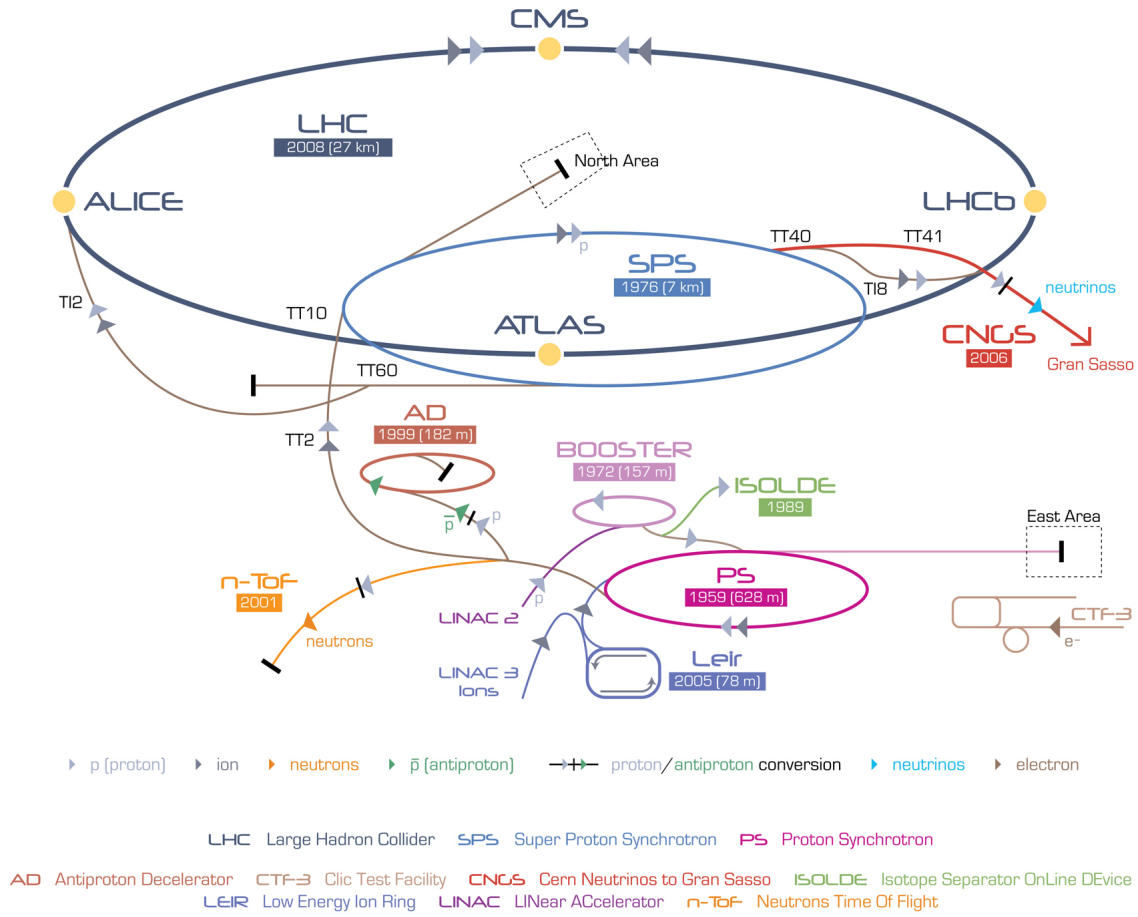


Figure 1–4: Large Hadron Collider (LHC).
The Accelerator Complex and its principal experiments. (Taken from [14]).

study, physics beyond the SM, rare new physics searches, among others. These detectors are located in two collisions points of the LHC.

- The ***Large Hadron Collider beauty*** (LHCb) experiment to study $b$ physics (hadrons containing $b$ quarks) and the asymmetry between matter and antimatter. ***A Large Ion Collider Experiment*** (ALICE) experiment has been especially designed to study heavy ions (Lead-Lead ($Pb - Pb$)) collisions and the "Quark-Gluon Plasma" which remained for a short time after Big Bang. These detectors are the other two collisions points.

- The ***Large Hadron Collider forward*** (LHCf) to study the production of particles in the forward region, the ***TOTal Elastic and diffractive cross section Measurement*** (TOTEM) experiment for the measurement of the proton elastic scattering at small angles (TOTEM is next to CMS) and the ***Monopole and Exotics Detector at the LHC*** (MOEDAL) to search directly for the magnetic monopole (a hypothetical particle with a magnetic charge). These experiments are not in collision points of the LHC.

In addition to the previously explained, in the LHC hadrons or ions collide and; due to particles in the accelerator have a very small size, it is very difficult to get a head-on collision. Consequently, $100,000$ million bunch of proton down to 64 $\mu m$ produce only about 20 collisions per crossing. Furthermore, since the bunches cross each other after every 25 $ns$ then around 600 million collisions per second are produced. However, many protons may not have a collision and keep on circulating in beam ring time after time [13].

Some of the principal concepts of the LHC collisions are described below.

- **Centre of Mass Energy** is the energy available in the collision $\sqrt{s}$. The LHC was designed for a centre-of-mass energy up to 14 $TeV$ ($14 \times 10^6$ $MeV$).
- **Cross section** refers to the likelihood of interaction between particles. Specifically, the area where the particle can interact with the other particles. The cross section $\sigma$ is measured in barns $b$ ($1b = 10^{-28} m^2$).
- **Luminosity** is a measure of the number of collisions that pass through a given area each second. In other words, the luminosity gives the number of collisions independent on how many particles there are in total and its units are $cm^{-2}s^{-1}$. The instantaneous luminosity can be defined as $L = \frac{\dot{N}_{evt}}{\sigma}$ where $N_{evt}$ is the number of events and $\dot{N}_{evt} = \frac{\partial N_{evt}}{\partial t}$. The integrated luminosity ($\mathscr{L}$) is a term which gives the amount of data which has been collected.

- **Event Rate** is the amount of events per unit time ($events/s$). Then, it can be calculated as $event\ rate = luminosity \times crosssection$.
- **Minimum Bias Events** is associated with non-single diffractive events (NSD). In collisions some of the protons are not smashed up or broken into pieces, these events are called "diffractive collisions". The experiments use the trigger (trigger is explained in the next chapter) to minimize these effects.
- **Pileup Events** refer to in one single bunch crossing may produce several separate events in high luminosity colliders like the LHC (separate collision vertex within the envelope provided by the colliding beams), and if the number of protons per bunch in time increase, then pileup events increase.
- **Operating conditions in the 2011 and 2012 periods**. The data analyzed in this thesis is taken from collisions produced in the 2011 year at the LHC. In the year 2011, the center-of-mass energy for proton-proton ($pp$) collisions was 7 $TeV$, the instantaneous luminosity was raised from low luminosities up to $L = 2 \times 10^{33} cm^{-2} s^{-1}$ and the mean pileup was $\langle N_{PV} \rangle = 8$ in a time spacing between each bunch crossing of 25 $ns$. Additionally, for the 2012 period, the center-of-mass energy for $pp$ runs was raised to 8 $TeV$, the instantaneous luminosity was reach at $8 \times 10^{33} cm^{-2} s^{-1}$ during the second part of the year and the mean 2012 pileup was $\langle N_{PV} \rangle = 21$.

# CHAPTER 2
# THE COMPACT MUON SOLENOID EXPERIMENT

The Compact Muon Solenoid (CMS) [15] experiment is one of the two large general-purpose detectors at the LHC. CMS is a big experiment, measuring 28.7 $m$ in length, 15 $m$ in diameter, and 14,000 $tons$ of weight. In addition, more than 3000 scientists, engineers, and students from 172 institutes in 40 countries work in this experiment.

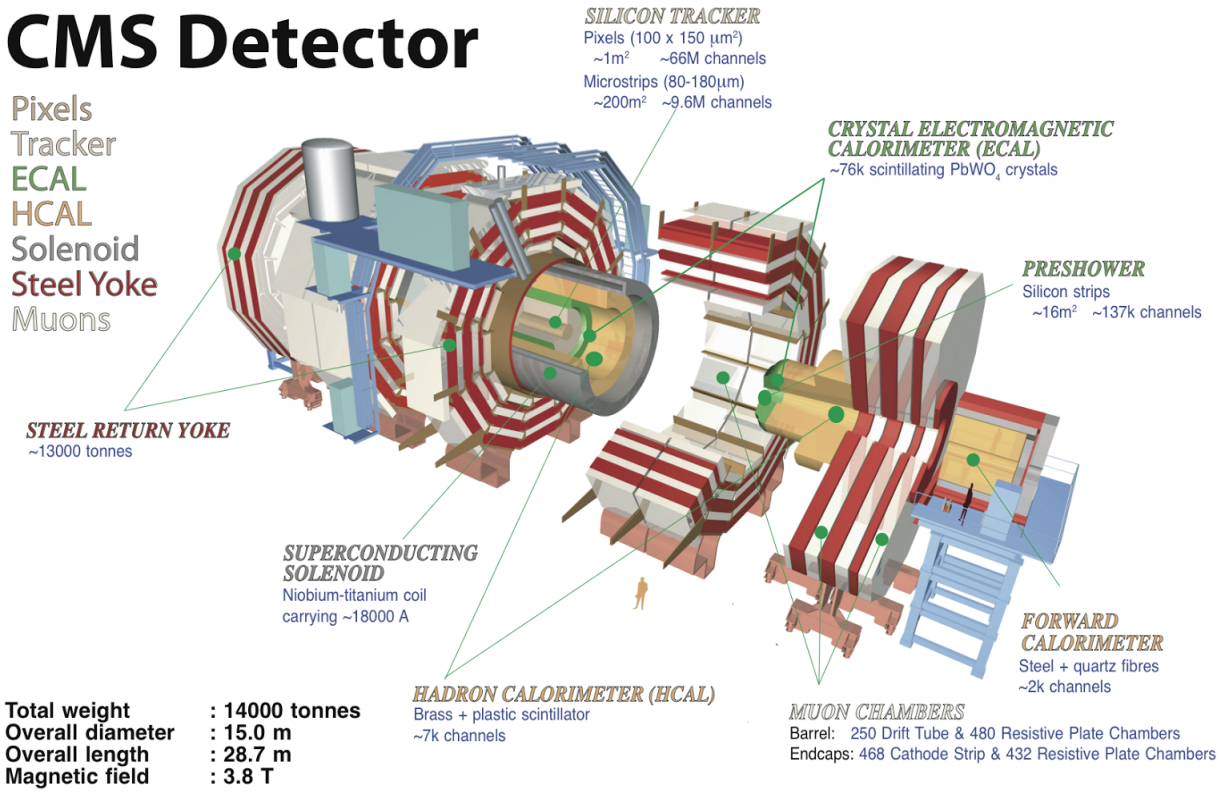


Figure 2–1: View of the CMS detector.
The LHC beams travel in opposite directions along the central axis of the CMS cylinder colliding in the middle of the CMS detector (Taken from [16]).

Due to the challenges of the LHC accelerator, CMS needs precise requirements and features. One of the most important requests is the magnetic field, which is generated by the superconducting solenoid with measurements of 13 $m$ long and 6 $m$ large. It generates a homogeneous 4 $T$ magnetic field along the beam direction. Inside of the solenoid are the silicon inner tracker and two calorimeters, and outside of the solenoid are the muon chambers (See Figure 2–1). Additionally, the requirements of the CMS detector [17] are summarized below.

- Good muon identification and momentum resolution over a wide range of momenta and angles. Also, good dimuon mass resolution ($\approx 1\%$ at $100 GeV/c^2$) and the ability to determine unambiguously the charge of muons with $p < 1\ TeV$.
- Good charged-particle momentum resolution and reconstruction efficiency in the inner tracker. And efficient triggering and offline tagging of $\tau$ and $b$-jets, requiring pixel detectors close to the interaction region.
- Good electromagnetic energy resolution, good diphoton and dielectron mass resolution ($\approx 1\%$ at 100 $GeV/c^2$), wide geometric coverage, $\pi^0$ rejection, and efficient photon and lepton isolation at high luminosities.
- Good missing-transverse-energy and dijet-mass resolution, requiring hadron calorimeters with a large hermetic geometric coverage and with fine lateral segmentation.

This chapter describes the main objectives of the CMS and provides an overview of the operation of each part of the detector and how data is acquired.

## 2.1 Physics Goals of CMS at the LHC

CMS is a multi-purpose detector; it was build to answer the biggest questions about our understanding of the Universe. The most important goals are:

- to explore physics at the large ($TeV$) energy scales.

- to study the properties of the Higgs Bosson. The principal result related to the Higgs Bosson was published on March 19 of 2013: *Observation of a new boson with mass near* 125 *GeV in pp collisions at* 7 *and* 8 *TeV of center-of-mass energy.*
- to study $b$ physics ($b$ hadrons decay) since the cross section in $pp$ collisions at the LHC center of mass energy is not negligible.
- to look for evidence of physics beyond the Standard Model, such as SuperSymmetry (SUSY), extra dimensions, among others.
- to study heavy ion collisions.

## 2.2 CMS Coordinate System

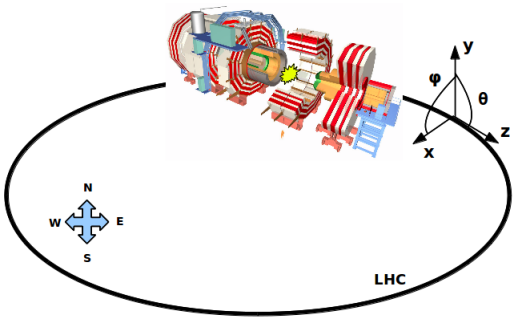


Figure 2–2: CMS global coordinate system with respect to the LHC.

The CMS coordinate system has its origin at the collision point inside of the detector (the center of the detector). The $x$ axis pointing radially towards the center of the LHC ring, the $y$ axis pointing vertically upwards, and the $z$ axis pointing along the beam direction (See Figure 2–2). Furthermore, the azimuthal angle $\varphi$ is the angle in the transverse plane ($xy$-plane) with respect to positive $x$-axis and the polar angle $\theta$ is measured with respect to the positive $z$-axis [17].

Other variables important to understand how the coordinate system of CMS works are the Rapidity, the Pseudorapidity, and the Transverse Momentum which are described below.

- **Rapidity** is an additive quantity under Lorentz transformations and is defined as $y = 1/2ln\left(\frac{E+P_z}{E+P_z}\right)$ where $p_z$ is the component of momentum along the beam axis and $E$ is the energy. This variable refers to the speed along the $z$ axis measured with the lab as the reference point [15].
- **Pseudorapidity** describes the angle of a particle with respect to the $z$-axis and is defined as $\eta = -ln\left(\frac{\theta}{2}\right)$, where $\eta$ only depends on the polar angle $\theta$.

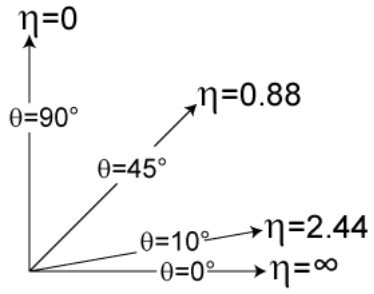


Figure 2–3: Pseudorapidity Values.

Pseuporapidity is zero if it is perpendicular to the $z$-axis and infinity if it is along the $z$-axis.

- **Transverse Momentum** is the magnitude of the momentum in the transverse plane $(xy)$ and is given by $p_T = \sqrt{p_x^2 + p_y^2}$.

## 2.3 CMS Detector Components

Around the collision point in the accelerators are the detectors that use electromagnetic fields to curve the path of the particle. They were designed with multi-components to measure different properties or type of particles and use electromagnetic fields to curve the path of the particles (See figure 2–4). Tracking devices reveal the path of charged particles; calorimeters stop, absorb and measure the particles energy; however, the neutrinos and muons can pass through all the chambers.

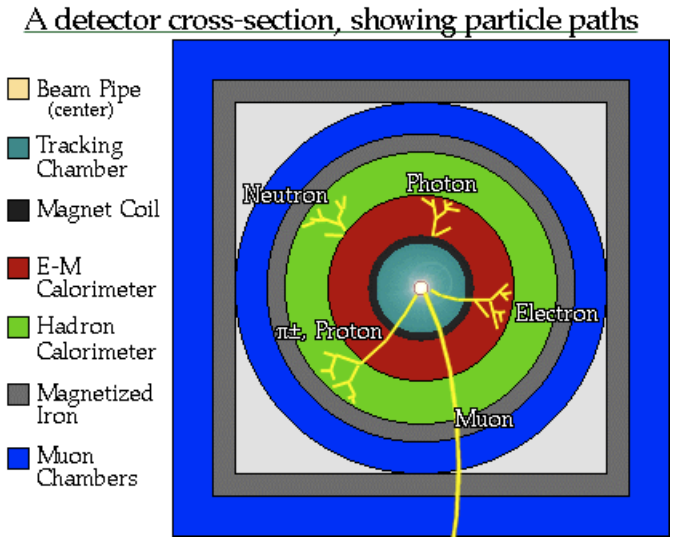


Figure 2–4: cross-section view of a detector. (Taken from [18]).

In this section, the main features of the Compact Muon Solenoid (CMS) are described, specifically, the inner tracking system, the calorimeters, the solenoid and the muon system.

### 2.3.1 The inner tracking system

The inner tracker [15] is around the LHC beam piper, and it has 5.8 $m$ in length and 2.8 $m$ in diameter. This system has been a challenge for scientists because of the LHC luminosity ($10^{34}\ cm^{-2}s^{-1}$) implies on average about $1,000$ particles from more than 20 overlapping $pp$ collisions each 25 $ns$ (bunch crossing). Thus, the detector was developed to have a minimum radiation damage due to the particle flux, with an expected lifetime of 10 years of operation.

In addition, it provides a precise and efficient measurement of the trajectories of charged particles, as well as a precise reconstruction of secondary vertices. To do this, the tracks of the particles are matched to the vertices from were they originated, taking

position by matching only a few accurate position measurements, the tracks can be suitably reconstructed. Furthermore, the momentum of the particle can then be measured from the reconstructed track inside of the magnetic field.

To get these requirements the CMS inner tracker has a pixel detector and a silicon detector which are described below.

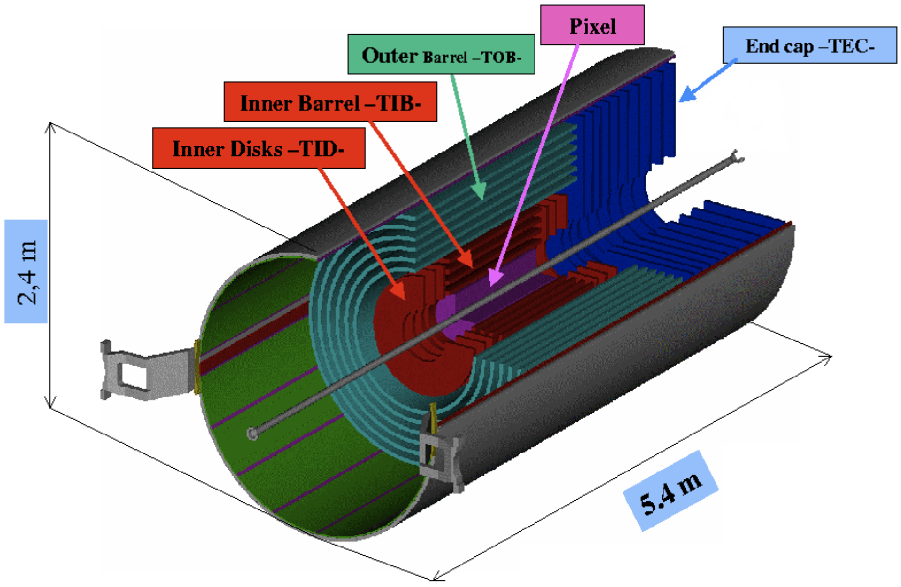


Figure 2–5: Pseudorapidity values.

- **Pixel Detector** is the most inner subdetector of CMS. This subdetector uses pixel detectors to get high spatial precision with hit resolutions between 9 and a few tens of $\mu m$ and to provide a fast response in the association of the hits with the correct bunch crossing. Specifically, the pixel detector provides three spatial measurement points which are used to initiate the track reconstruction for charged particles and to identify primary vertices in the entire central tracker (pseudorapidity range of $|\eta| = 2.5$). This detector consists of the barrel (BPIX) and the forward (FPIX). On one side, BPIX consists of three barrer layers at radii between 4.4 $cm$, 7.3 $cm$ and 10.2 $cm$ and extends

53 $cm$ along the $z$-axis; and on the other, FPIX consists of two disks of pixel modules at radii between 6 $cm$ to 15 $cm$ and are installed at $z = \pm 34.5$ cm and $z = \pm 46.5 cm$ [19].

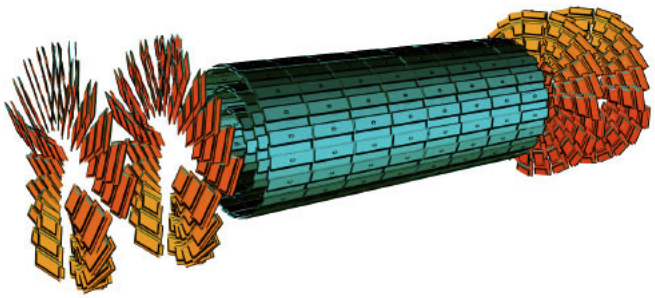

Figure 2–6: Pixel Detector

- **Silicon Strip Tracker** [19] covers the radial region between 20 $cm$ and 116 $cm$, and consists of three systems: the Tracker Inner Barrel (TIB) and Disks (TID), the Tracker Outer Barrel (TOB), and the two Tracker EndCaps (TEC+, TEC-). Its architecture is modular with a thickness of 320 $\mu m$ and 500 $\mu m$. The inner part implements micro-strips with a pitch of 80 $\mu m$ in the innermost layers and $120 \mu m$ in the outermost layers. Furthermore, the deposited charges drift transversely in the sensor material due to the intense magnetic field, including in a set of adjacent cells (digis). The offline local reconstruction identifies sets of adjacent digis to form a single hit for a particle. The hit position is finally determined as the charge-weighted average of all the strip positions, corrected by the Lorentz angle. The uncertainty is estimated with a quadratic function of the cluster width projected on the sensor in the plane perpendicular to the strip modules.

### 2.3.2 The Calorimetry

Calorimeters [15] are detectors that measure the energy of the particles. When the particles enter to the calorimeter, they initiate a particle's shower and their energy is collected by the calorimeter. There the electrons, photons and hadrons are stopped, and muons and tau leptons deposit a very small part of their energy; the muons are

detected using the tracking and muon detector subsystems. The first calorimeter (Electromagnetic Calorimeter) was designed to measure the energies of electrons and photons with high precision and the second calorimeter (Hadronic Calorimeter) detects hadrons. Furthermore, neutrinos are not detected directly, but can be inferred of missing energy in the decays.

**Electromagnetic calorimeter (ECAL)**

ECAL [15] is composed of a barrel and two endcaps which cover pseudorapidity ranges of $|\eta| < 1.479$ and $1.479 < |\eta| < 3.0$ respectively. The barrels are made of lead tungstate ($PbWO_4$) crystals, characterized by high density, short radiation length and fast response, combined with a sufficient radiation hardness. These particles produce electromagnetic showers of $e^-e^+$ pairs in the material, which are deflected by the electric field and cause the radiation of photons. Then, the photons produce $e^-e^+$ pairs, which radiate more photons. Finally, the energy of the incident particle is proportional to the number of $e^-e^+$ pairs produced (See Figure 2–7).

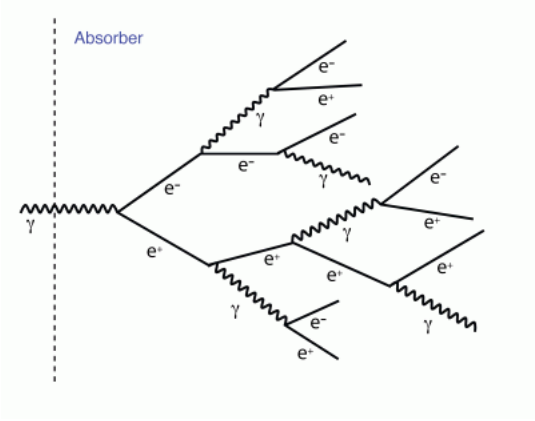


Figure 2–7: Electromagnetic shower.
(Taken from [20]).

In the calorimeter, the avalanche of photons produced is collected by photodiodes in the barrel and vacuum phototriodes in the endcaps. A fine-grained lead-silicon preshower

detector is installed in front of the ECAL endcaps with the purpose of distinguishing between prompt photons and neutral pion decays.

**Hadron Calorimeter (HCAL)**

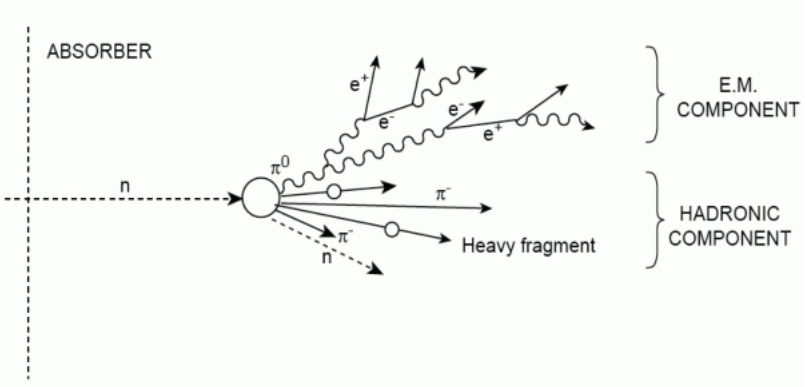


Figure 2–8: Hadronic shower
(Taken from [20]).

HCAL [15] measures the total energy of the hadrons, similar to the electromagnetic showers. Inside, the hadrons interact with nuclei of the detector matter due to the strong force, giving a shower of secondary particles. The production of hadronic showers is more complicated due to the fact that the shower has both hadronic and electromagnetic components (See Figure 2–8). It is located between the ECAL and the superconducting magnet in the radial distance range between 1.77 $m$ and 2.95 $m$. The barrel part covers the region $|\eta| < 1.3$ and the endcaps cover up to $|\eta| = 3.0$. Furthermore, the coil increases the material thickness in the barrel pseudorapidity region, such that the hadronic showers are fully absorbed before reaching to the muon system.

### 2.3.3 Superconducting Magnet

The superconducting solenoid [15] of 13 $m$ in length, 6 $m$ in diameter and $12,000$ $ton$, which saturates a 1.5 $m$ iron yoke to generate an intense magnetic field of 4 $T$. In fact, this solenoid gives to CMS its name. This superconducting magnet is made of a superconducting coil, the magnet yoke, a vacuum tank and ancillaries such as

cryogenics, power supplies and process controls. Inside of the bore of the magnet sits the inner tracker and the calorimetry, while outside are the flux return system and muon detection.

### 2.3.4 The Muon System

The muon system is the last subdetector of CMS and is the least exposed to the high particle fluencies of the collision beam. Four muon stations interleaved with iron return yokes plates of the magnet system provides a completely reconstruction in all the pseudorapidity range [15].

The only particles capable of reaching at the muon system are the muons and the neutrinos. However, the neutrinos rarely interact with the matter. Then, the measurements of this detector are from muons which are very important in the reconstructions of primary decays.

The muon stations [15] of the detector are made of several layers of aluminium drift tubes (DT) in the barrel region and cathode strip chambers (CSCs) in the endcap, which are used to measure the muon's position and momentum. Also, the detector has resistive plate chambers (RPCs), which provides information for the Level-1 trigger (This Trigger will be explained in the Section 2.5)

## 2.4 CMS Upgrade

The requirements of the LHC imply improvements, repairs and upgrades in the CMS detector. The LHC operations [21] started at 7 $TeV$ center of mass energy in 2011 and 8 $TeV$ in 2012, then shut down for 1.5 to 2 years to make the revisions necessary to run at 14 $TeV$. After this time, LHC will start operation in 2015, and in 2017-2018 have a long shutdown to prepare the LHC to operate at and eventually above the design luminosity of $10^{34} cm^{-2} s^{-1}$, rising gradually during this period to $2 \times 10^{34} cm^{-2} s^{-1}$.

Currently, the LHC is in the first shutdown, and some of the principal improvements in the CMS [21] are:

- The pixel detector will be replaced, due to this detector being designed for $1\times10^{34}cm^{-2}s^{-1}$ and needing to work in a luminosity of $2\times10^{34}cm^{-2}s^{-1}$. Thus the principal changes in this detector are: i) the three barrel layers (BPIX) and the two endcap discs(FPIX) will be changed by four barrel layers and three endcap discs. ii) Its weight will be reduced changing to $CO_2$ cooling and connections out of tracking volume. iii) Development of high bandwidth readout electronics and links as well as DC-DC power converters, which allow the reuse of existing fibers and cables and new readout chip with reduced data loss at higher collision rates.
- In the HCAL the photomultipliers (PMTs) will be changed with other PMTs with thinner glass windows and metal envelops, in order to reduce the Cherenkov radiation produced by the particles that travel through the glass, reject the false signals and improve the efficiency. Also, it will implement a depth segmentation to resist the higher luminosities and to compensate for the radiation damage of the scintillators.
- A new muon trigger will be developed in the muon system to deliver the additional muon tracks at high luminosity, also a layer of chambers will be added to improve the Level 1 of the trigger and to preserve the low momentums.

## 2.5 Trigger and data acquisition system

At the CMS, one billion of collisions are produced each second but only around 400 events can be stored. In addition, not all the events are necessary (minimum bias events) [22]. Then, the triggers are used to reduce the size of the data, which are stored in the machines.

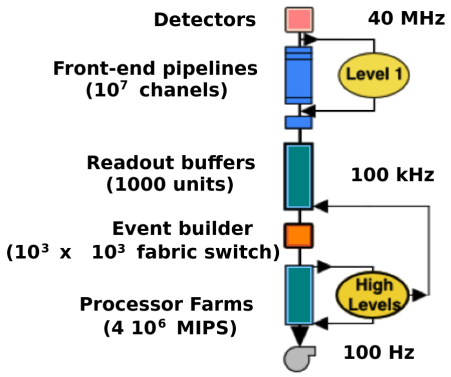


Figure 2–9: Trigger and data acquisition architectures at CMS. (Taken from [23]).

The trigger system must ensure high data recording efficiency for a wide variety of physics objects and event topologies, while applying very selective requirements (See Figure 2–9). Two different trigger levels are employed at CMS[22].

**Level-1 Trigger** (L1T), is implemented using custom electronics and is designed to reduce the event rate from 40 $MHz$ to 100 $kHz$. This trigger needs to take decisions for each bunch crossing within 3.2 $\mu s$. The L1 trigger is related to the identification of electrons, muons, photons, jets and missing transverse energy, combining the output of the L1 Calorimeter Trigger and L1 Muon Trigger.

**The High Level Trigger** (HLT) uses software reconstruction and Itering algorithms running on a large computing cluster. HLT reduces the L1 output rate down to the nominal rate of 100 $Hz$.

The Data Acquisition (DAQ) [24] system is integrated between the two stages of the trigger system, and can be summarized as follows:

- A signal is accepted and received by L1.
- The signal reads out the front-end electronics, combines the data into the proper event format and transmits them to the HLT farm for the second trigger selection.

- It forwards data to the online data quality monitoring system (DQM), which allows the monitor to get the quality of data from all subdetectors in real time, and transfers the information of HLT accepted events to storage in the CERN computing facilities.
- The output data are in RAW format which contains the information about the signals deposited in the detector's modules.
- Before being used for physics analyzes, they have to be further processed by a set of software programs performing the event reconstruction.

## 2.6 CMS Analysis Framework

The amount of data produced in the CMS is around 15 $TB$ per day. The data is reconstructed, analyzed and stored using a network [25] of computing centers,“ the LHC computing grid" or "WWCG". Computing sites are organized in a tiered structure, with the tier 0 being the CERN Computer Center, responsible for the first (prompt) reconstruction of the raw data, performed within 48 hours after the data recording. CMS uses CMSSW (Compact Muon Solenoid Software) for data analysis, which is constantly revised and extended. Following are the main CMSSW elements:

- Framework and Event Data Model (EDM) is used to modularize the software, which allows the development of each component independently. The process between data and the event is described by the Event Data Model (EDM). When events pass through different modules, they can read the data from the events or add to it. The framework uses different types of modules such as Pool source, EDProducer, EDFilter, EDAnalyzer, EDLooper and Output module.
- Simulation is a generator interface that incorporates different kinds of generators ( Pythia, Powheg, Mad-graph), and detector simulation can also be done using generator interface.
- Reconstruction of physical quantities (such as leptons or jets) between the information collected by the detector is called reconstruction. At CMS, there are three types

of reconstruction: local reconstruction, global reconstruction and combined physics objects.

- Analysis Tools according to the analysis requirements. Physics Analysis Toolkit (PAT) is created by Physics Analysis Groups (PAG) to be a general-purpose product. It is a high-level analysis layer where the ID algorithms and reconstructed objects are included. Physics objects can be selected and cleaned in this process to eliminate the objects with poor quality.

# CHAPTER 3
# OBJECTIVES

The research interests of the High Energy Physics (HEP) group of the University of Puerto Rico at Mayaguez Campus in the CMS experiment are focused on the search of new physics in rare $b$ baryon decays, precision test measurements of the Standard Model and pixel tracking detector performance. In particular, we collaborate in the CMS upgrade tracking simulation and the B physics groups as well as in the hardware development group.

Specifically, in this thesis the baryon $\Xi_b^-$ which is composed of $d$, $s$ and $b$ quarks is studied. This baryon is reconstructed through the final state $\Xi_b^- \rightarrow J/\psi\Xi^-$ with $J/\psi \rightarrow \mu^+\mu^-$, $\Xi^- \rightarrow \Lambda^0\pi^-$ and $\Lambda^0 \rightarrow p\pi^-$. The topology of this decay is shown in Figure 3–1.

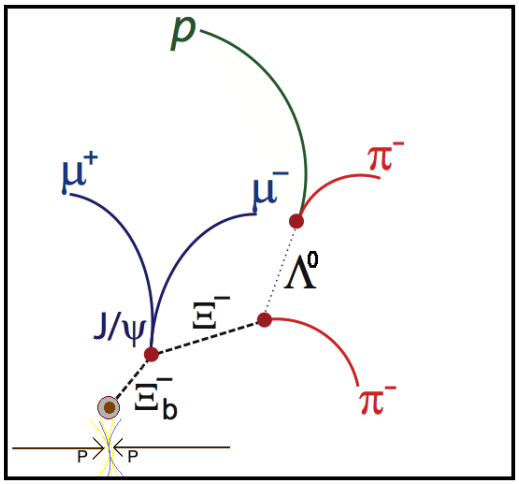


Figure 3–1: $\Xi_b^-$ chain decay.

A preliminary lifetime measurement of the $\Xi_b^-$ is presented in this thesis, using 5.1 $fb^{-1}$ of integrated luminosity from proton-proton collisions at center-of-mass energies at 7 $TeV$ of data acquired by the CMS experiment in 2011 at the LHC.

Therefore, the lifetime is found using proper time histograms which are made of the results of the data reconstructed, one from the signal region and two from the sidebands (right and left) of the invariant mass, i.e. three histograms are used to measure the lifetime: one of true events from the signal region and two of background events from the sidebands. The background events are five standard deviations away of the nominal mass of the $\Xi_b^-$. Finally, the technique to measure the $\Xi_b^-$ lifetime is a binned likelihood fit [26] on the proper time histograms.

# CHAPTER 4
# DATA RECONSTRUCTION, SELECTION AND MEASUREMENT OF THE $\Xi_b^-$ LIFETIME

This thesis presents a preliminary measurement of the $\Xi_b^-$ baryon lifetime with data collected by CMS during 2011 at 7 $TeV$, corresponding to 5.1 $fb^{-1}$ of integrated luminosity. The full decay chain studied is $\Xi_b^- \to J/\psi\Xi^-$ with $J/\psi \to \mu^+\mu^-$, $\Xi^- \to \Lambda^0\pi^-$ and $\Lambda^0 \to p\pi^-$, where:

- The $\Xi_b^-$ particle comes from a primaty vertex ($PV$).
- $\Xi_b^- \to J/\psi\Xi^-(J/\psi \to \mu^+\mu^-)$ at a secondary vertex ($SV_{J/\psi}$).
- $\Xi^- \to \Lambda^0\pi^-$ at a vertex ($SV_{\Xi^-}$) . The charged pion from this decay is labeled $\pi^-_{\Xi^-}$.
- $\Lambda^0 \to p\pi^-$ at a vertex ($SV_{\Lambda^0}$). The charged pion from this decay is labeled $\pi^-_{\Lambda^0}$.

In this chapter the reconstruction and selection processes are described, in addition to the description of the $\Xi_b^-$ lifetime measurement.

## 4.1 Reconstruction Process

CMS is used to identify and reconstruct particles arising from $pp$ collisions at LHC with the combination of the information from all the subdetectors. Therefore, the reconstruction process needs to be done carefully to choose well in the large amount of data. This section presents the stages done to reconstruct the $\Xi_b^-$ candidates (See Figure 4–1).

- Muons are identified by matching tracks reconstructed in the inner tracker with track segments in the muon spectrometer, which are consistent with the muon trajectory. To get the signal of the $J/\psi$ the following is needed:
  1. Combine two oppositely charged muons ($\mu^+\mu^-$) with a common vertex.

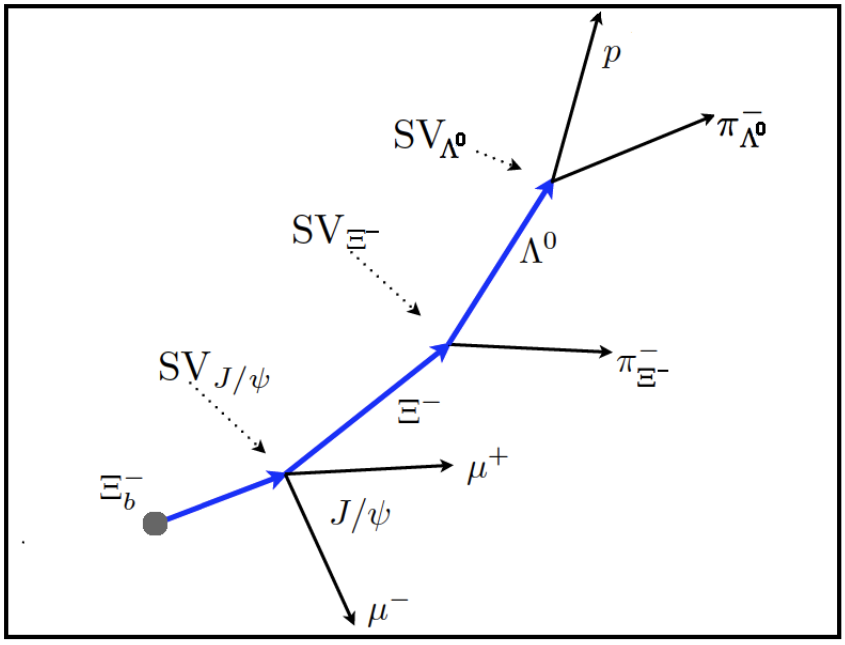


Figure 4–1: $\Xi_b^-$ decay reconstruction.

2. The muons used are Global Muons which use an "outside-in" approach. Starting from a standalone reconstructed muon which is obtained from the offline reconstruction, the segments reconstructed in the muon chambers are used to generate "seeds" consisting of position and direction vectors and an estimate of the muon transverse momentum. Then, the muon trajectory is extrapolated from the innermost muon station to the outer tracker surface. Silicon layers compatible with the muon trajectory are then determined, and a region of interest within them is defined in which to perform regional track reconstruction. The determination of the region of interest is based on the track parameters and their corresponding uncertainties of the extrapolated muon trajectory, obtained with the assumption that the muon originates from the interaction point. If the matching is valid, the combined track is a Global Muon.

- $\Lambda^0$ candidates are reconstructed from two oppositely charged tracks that originate from a common vertex ($p$ and $\pi^-_{\Lambda^0}$). These candidates are taken from the experiment software collection with:
  1. A minimum impact parameter (perpendicular distance to the closest approach if the particle were undeflected) of every daughter with respect to the beam spot of 0.5 $\sigma$.
  2. 5 $\sigma$ distance between the vertex position and the beam spot.
  3. The $\Lambda^0$ candidates require a mass window of 10 $MeV/c^2$ around the nominal value (115.683 $MeV/c^2$).
- $\Lambda^0$ candidates are then combined with negatively charged tracks corresponding to $\pi^-_{\Xi^-}$ to form $\Xi^-$ candidates.
- The $\Lambda^0$ and $\pi^-_{\Xi^-}$ tracks require a common vertex.
- $\Xi^-$ and $J/\psi$ candidates originated from a common vertex form $\Xi^-_b$ candidates.

Therefore, using the above steps the $\Xi^-_b$ particle candidates are obtained; however, in order to reduce the background it is necessary to use more restrictive selection cuts, which are described in the next section.

## 4.2 Selection Process

In the selection process, different cuts are used to maximize the signal and minimize the background. In this thesis, each cut was studied to improve the result and the final cuts are explained below.

**Mass Window Cut**

The background in the sample is made of possible candidates of particles from the real data, which can be cleaned using the particle's mass of the candidate. Therefore, an invariant mass cut around of the particle's mass given by the PDG [9] is done. In other words, the invariant mass window allows us to select only the candidates that are reasonably close to the particle mass and the background has to be lowered (it means reject possible events which are not our candidate to be the particle).

**Transversal Momentum $p_T$**

In the experiment, some of the protons may not collide at the interaction point and they stay in the pipe. Therefore, the momentum along the beam line may be left over from the beam particles and to clean the signal it is better to use the perpendicular momentum to the beam line. Then, the transversal momentum $p_T$ is the component perpendicular to the beam line. It corresponds to $p_T = \sqrt{p_x^2 + p_y^2}$ and is well associated with the particles from the collision.

**Vertex Confidence Level $CL$**

The tracks do not intersect exactly to form vertices in the reconstruction process; then, the vertices are formed with a confidence level $CL$. It is the probability that an observation will give rise to a chi-squared larger than the one observed; i.e. $CL$ is the probability of how likely is to observe as high (or higher) a chi-squared. This variable can be used to clean the signal, in fact, the minimal cut on the $CL$ value is required to be greater than 1 %.

**Vertex Separation Significance $L/\sigma_L$**

The vertex separation significance $L/\sigma_L$ is a measure of the separation significance between the vertices, where $L$ is the distance between the vertices and $\sigma_L$ is the uncertainty in $L$. This variable can reduce the background because it helps to identify the correlation between vertices.

**Cosine of the decay angle** *cos* $\alpha$

The cosine of the decay angle *cos* $\alpha$, where $\alpha$ is the angle between the momentum vector and the displacement vector of the particle. It is used to discriminate the signal and the background, or the correlations; due to the momentum and the displacement must have the same direction ($cos\ \alpha \approx 1$).

The $\Xi_b^-$ signal was cleaned using the cuts described above and the plots of each cut is shown in order to verify the cuts done.

- $p_T(p) > 0.5\ GeV$ for the proton from the lambda (See Figure 4–2).

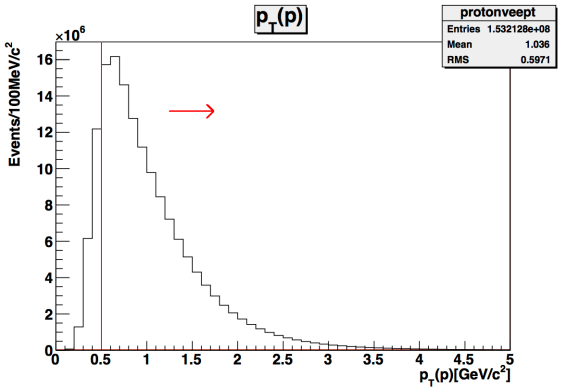


Figure 4–2: Transversal Momentum of all proton candidates.

- $p_T(\pi^-_{\Lambda^0}) > 0.3\ GeV$ for the pion from the lambda (See Figure 4–3).

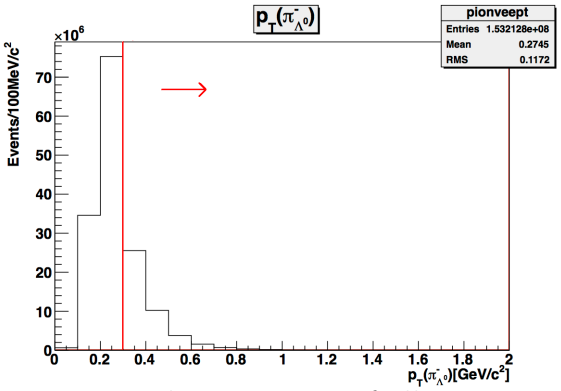


Figure 4–3: Transversal Momentum of all pion $\pi^-_{\Lambda^0}$ candidates.

- A veto mass window cut to the $K_s^0$ candidates of 10 $MeV/c^2$ around the nominal mass (497.61 $MeV/c^2$) is applied, due to $K_s^0$ can decay into $\pi^+\pi^-$ and may be confused with a $\Lambda^0$ candidate (See Figure 4–4).

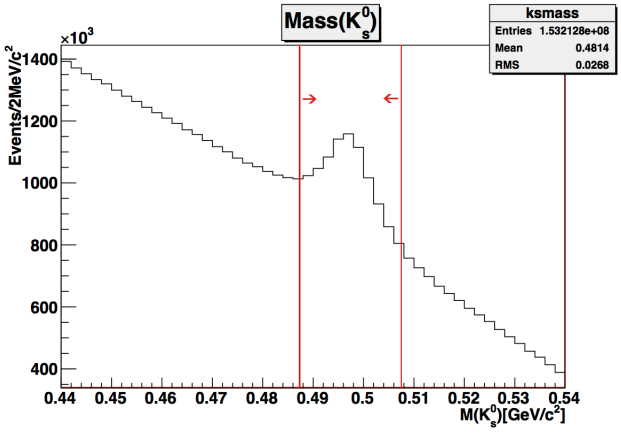


Figure 4–4: Veto mass window cut of all the $K_s^0$ candidates.

- Select $\Lambda^0$ candidates with a mass window cut of 6 $MeV/c^2$ around the nominal value (115.683 $MeV/c^2$) (See Figure 4–5). Appendix A contains the plots with the events that are not chosen in this cut to prove the good selection of the mass window cut.

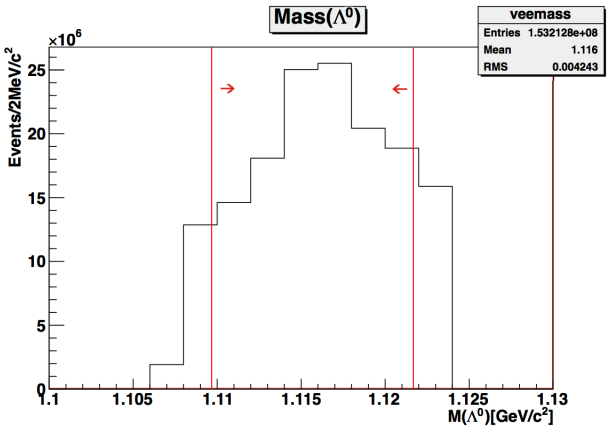


Figure 4–5: Veto mass window cut of the $\Lambda^0$ candidates.

- Combine $\Lambda^0$ candidates with $\pi^-_{\Xi^-}$ tracks candidates to form $\Xi^-$ candidates.
- The $\pi^-_{\Xi^-}$ candidates require a transversal momentum $p_T(\pi^-_{\Xi^-}) > 0.3\ GeV$ (See Figure 4–6).

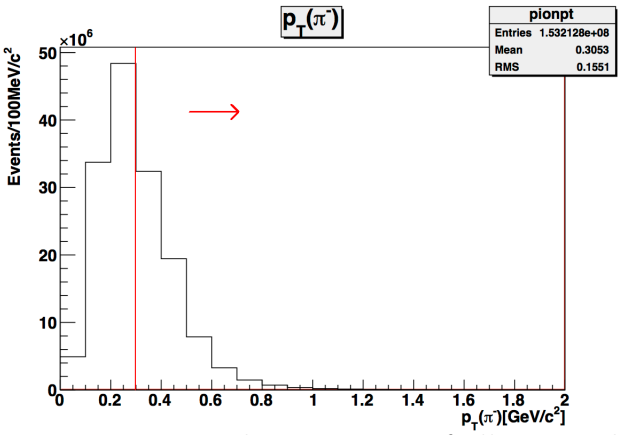


Figure 4–6: Transversal Momentum of all $\pi^-$ candidates.

- Vertex ($\Xi^-$) with $CL > 0.1$ (See Figure 4–7).

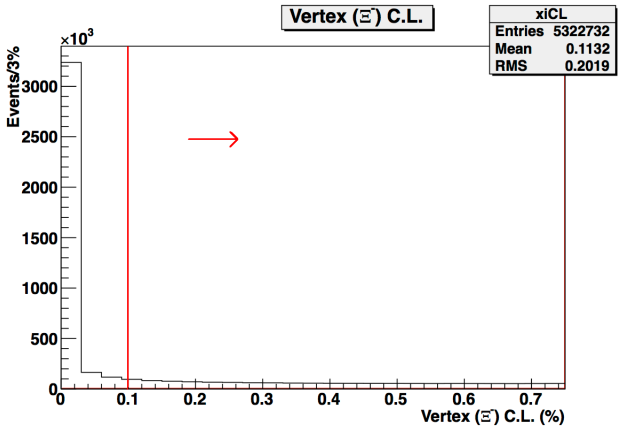


Figure 4–7: Vertex ($\Xi^-$) CL of all the $\Xi^-$ candidates.

- $\Xi^-$ candidates have a mass window cut of 10 $MeV/c^2$ around the PDG value (1321.7 $MeV/c^2$) (See Figure 4–8).

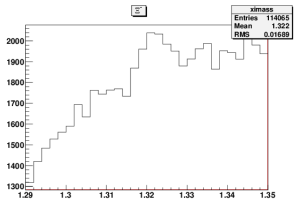


Figure 4–8: Veto mass window cut of the $\Xi^-$ candidates.

- Combine $\Xi^-$ candidates with $J/\psi$ candidates out of two muons (trigger matched).
- $J/\psi$ candidates require transversal momentum $p_T(J/\psi) > 4\ GeV$ (See Figure 4–9).

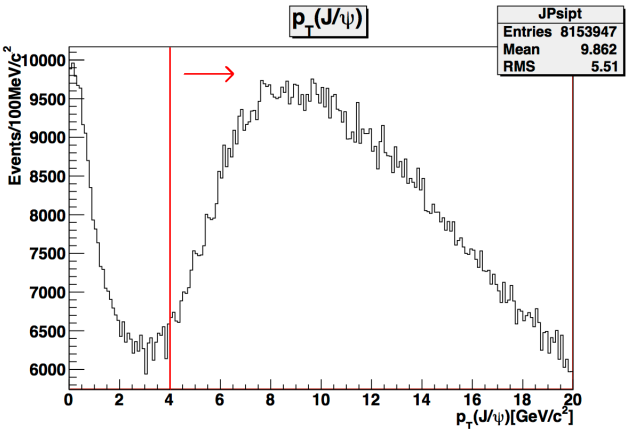


Figure 4–9: Transversal Momentum of all $p_T(J/\psi)$ candidates.

- The $\mu^+\mu^-$ mass window cut of 50 $MeV/c^2$ around the nominal value (3096.16 $MeV/c^2$) (See Figure 4–10). Appendix B contains the plots with the events that are not chosen in this cut to prove the good selection mass window cut.

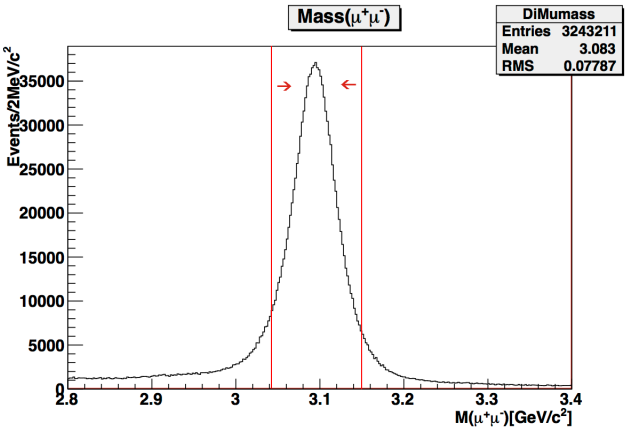


Figure 4–10: Veto mass window cut of the $\mu^+\mu^-$ candidates.

- The $\Xi^-$ trajectory not being more than 3 $\sigma_L$ away from the $J/\psi$ vertex(See Figure 4–11).

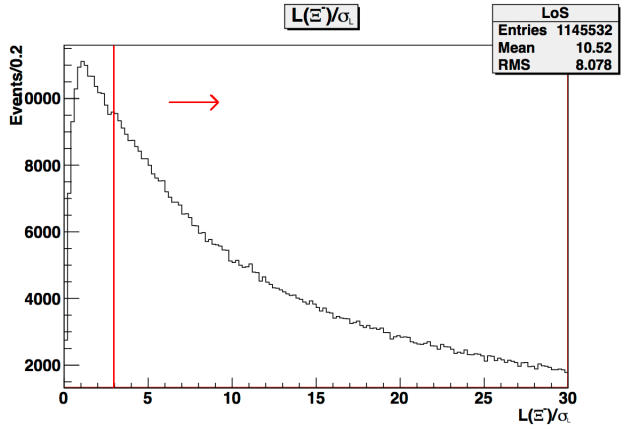


Figure 4–11: $L(\Xi^-)/\sigma_L$ cut of the $\Xi^-$ candidates.

- $\Xi_b^-$ candidates are required to have $p_T > 10\ GeV$(See Figure 4–12).

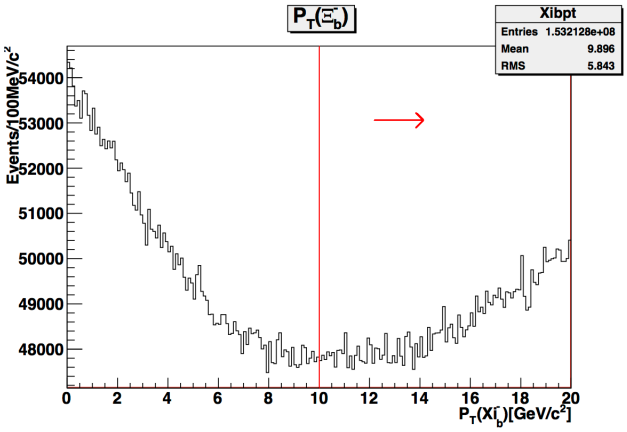


Figure 4–12: Transversal Momentum of all $\Xi_b^-$ candidates.

- $cos\ \alpha > 0.9$ for the $\Xi_b^-$ candidates (See Figure 4–13).

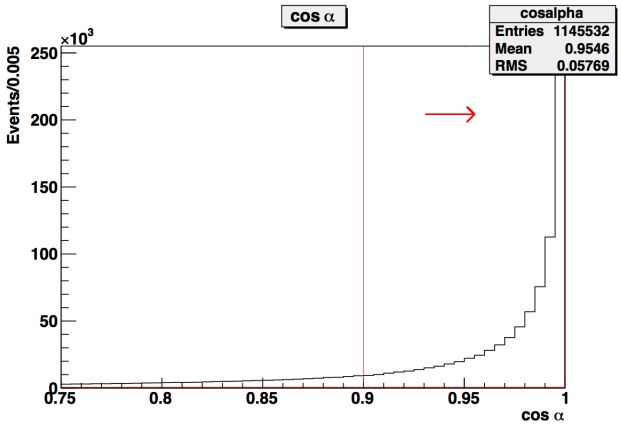


Figure 4–13: $cos\ \alpha$ cut of the $\Xi_b^-$ candidates.

- $\Xi_b^-$ candidates are required to have $L(\Xi_b^-)/\sigma_L > 4$.

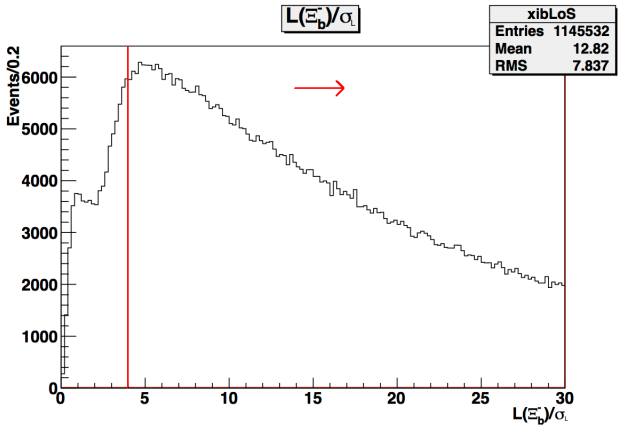


Figure 4–14: $L(\Xi_b^-)/\sigma_L$ of all the $\Xi_b^-$ candidates.

Table 4–1: Specific cuts in the selection process of the $\Xi_b^-$ candidates.

| Cut | Value |
|---|---|
| $p_T(p)$ | $> 0.5\ GeV$ |
| $p_T(\pi^-_{\Lambda^0})$ | $> 0.3\ GeV$ |
| $K^0_s$ veto mass | $0.497 \pm 0.010\ GeV/c^2$ |
| $\Lambda^0$ mass | $1.115 \pm 0.006\ GeV/c^2$ |
| $p_T(\pi^-_{\Xi^-})$ | $> 0.3\ GeV$ |
| Vertex $(\Xi^-)$ $CL$ | $> 0.1$ |
| $\Xi^-$ mass | $1.321 \pm 0.010\ GeV/c^2$ |
| $\mu^+\mu^-$ mass | $3.096 \pm 0.050\ GeV/c^2$ |
| $p_T(J/\psi)$ | $> 4\ GeV$ |
| $L(\Xi^-)/\sigma_L$ | $> 3$ |
| $p_T(\Xi_b^-)$ | $> 10\ GeV$ |
| $cos\ \alpha$ | $> 0.9$ |
| $L(\Xi_b^-)/\sigma_L$ | $> 4$ |

To summarize the specific cuts are in the Table 4–1. For other side, in some studies, the mass constraints can be less restrictive. For example, the mass window cut of the $\Lambda^0$ may be of 8 $MeV/c^2$ around of its nominal value, and the $\mu^+\mu^-$ mass window cut may be of 150 $MeV/c^2$ around of its nominal value. In this thesis, the windows cuts are chosen due to we believe that the events missing are part of the background; however, the selection process can be done using less restrictive mass constraints.

### 4.2.1 2011 Data Sample Results

The data used in this thesis was collected in the 2011 year. This data was divided into two run periods: 2011A and 2011B. The instantaneous luminosities of these periods are summarized in the Table 4–2.

Table 4–2: Instantaneous Luminosities of the two periods of data taken in the 2011 year at CMS.

| Period | Instantaneous Luminosities $cm^{-2}s^{-1}$ |
|---|---|
| 2011A | $5 \times 10^{32}$, $1 \times 10^{33}$, $1.4 \times 10^{33}$, $2 \times 10^{33}$, $3 \times 10^{33}$ |
| 2012B | $5 \times 10^{33}$ |

A run is composed of many lumisection, where lumisection is a fixed range of time of a run of data acquisition (90 seconds aproximately) during which time the instantaneous Luminosity of LHC is assumed not to change. However, not all the lumis are good data, then they are selected and organized by lumimask files and are called JSON files, each containing the list of valid run and lumisection for a certain data acquisition period.

Specifically, in this measurement is used the MuOnia data samples, produced centrally and based on data recorded with the CMS detector. The MuOnia data samples contain information of reconstructed physics objects like electrons, muons, jets, among others, for every event. The Appendix C contains the specific paths of the data samples and the JSON files used.

Table 4–3: Dimuon Triggers

| Trigger Path | $L$ | $p_T$ | $CL$ | $\|\eta\|$ |
|---|---|---|---|---|
| | $(pb^{-1})$ | $GeV$ | % | |
| $HLT\_DoubleMu3\_Jpsi\_Displaced$ | 923.83 | 3.5 | 15 | |
| $HLT\_Dimuon6p5\_Jpsi\_Displaced$ | 174.7 | 6.5 | 10 | $< 1.3$ |
| $HLT\_Dimuon7\_Jpsi\_Displaced$ | 985.05 | 3.5 | 10 | |

Furthermore, triggers were used to select the data. The muon candidates are required to pass the trigger with at least $|\eta| < 2.4$ and other characteristics of the triggers

used are summarized in the Table 4–3, where $L$ refers to the luminosity, $p_T$ is the momentum of the muons, $CL$ is the vertex confidence level and $\eta$ is the pseudorapidity.

The final candidates after the reconstruction and selection processes of the $\Xi_b^-$ particles are show in the Figure 4–15. A total of 63 candidates were measured with a mean mass value of $5.798 \pm 0.015\ GeV/c^2$, where the fit used to analyze the mass distribution is a Gauss Fuction and a Linear Function for the background.

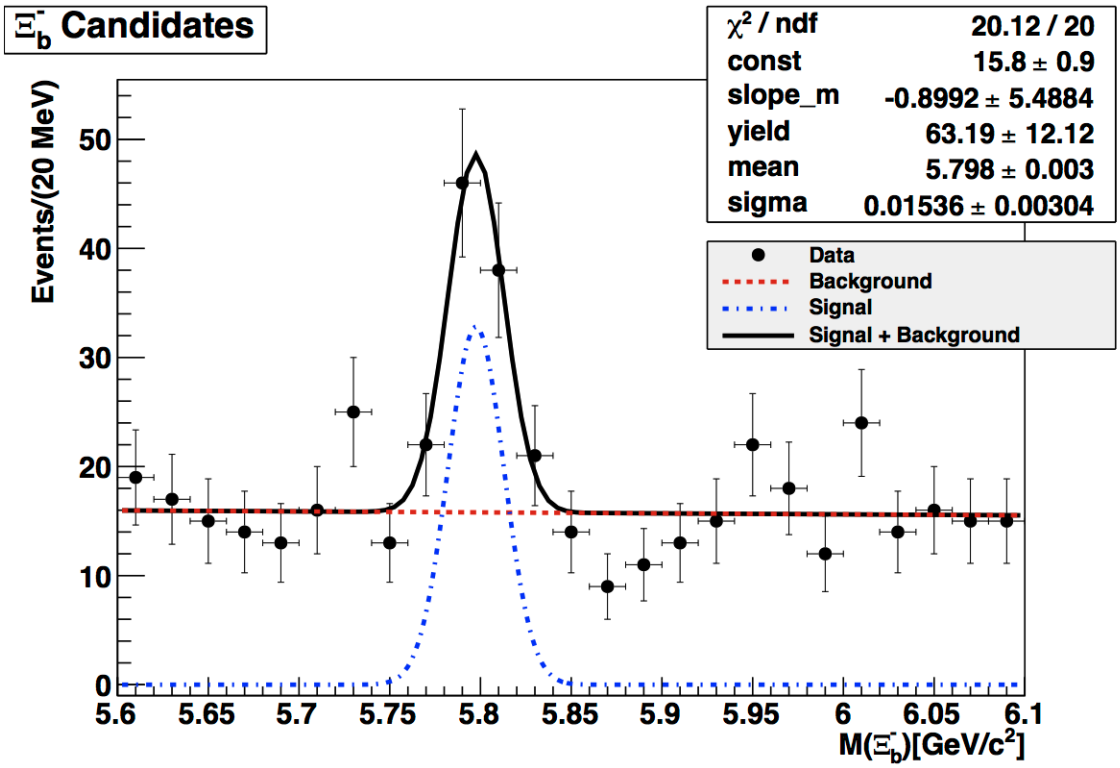


Figure 4–15: $\Xi_b^-$ Candidates.

### 4.3 Measurement of $\Xi_b^-$ lifetime

It is possible to measure the lifetime of short lived charged particles because of the good separation between the vertices. In this section, the method used to measure the lifetime and the results of the $\Xi_b^-$ particle is described.

The relativistic decay time in the center of mass frame is expressed as:

$$t = \frac{L}{c\beta\gamma} \tag{4.1}$$

where $L$ is the flight distance in three dimensions, $c$ is the speed of light ($c = 3\times10^8 m/s$), $\beta$ is the ratio between the decaying particle velocity and the speed of light ($\beta = v/c$), and $\gamma$ is the Lorentz boost factor $\gamma = 1/\sqrt{1-\beta^2}$. Furthermore, the decay time distribution can be expressed for each individual event by a probability density function [27] following the exponential decay law:

$$f_t = \frac{1}{\tau} e^{-t/\tau} \tag{4.2}$$

where $\tau$ is the mean lifetime of the particle.

In addition, in this study the fit of reduced proper time ($t'$) is done, which is defined as

$$t' = \frac{L - N\sigma_L}{c\beta\gamma} \tag{4.3}$$

where $N$ is the vertex detachment cut which refers to the $L(\Xi_b^-)/\sigma_L$ cut in the selection process and $\sigma_L$ is the standard desviation of the measurement of $L$. In this thesis we used $N = 2, 3, 4, 5, 6, 7$.

Table 4–4: Units at the experiment.

| | Unit |
|---|---|
| $L$ | $cm$ |
| $\sigma_L$ | $cm$ |
| $t$ | $cm$ |
| $E$ | $GeV/c^2$ |
| $p$ | $GeV/c$ |
| $v$ | Dimensionless |

The relation $p = \gamma m v$ (where $p$ and $m$ are the momentum and the invariant mass of the particle respectively) is used to determine $c\beta\gamma$, due to $p/m = \gamma v$ which is the same

as $p/m = c\beta\gamma$. Furthermore, the experiment uses natural units which are summarized in the Table 4–4; however, the reduced proper time histograms are done in $ps = 10^{-12}$ $s$ which are obtained doing the conversion (dividing by the speed of light to get seconds an multiplying by $10^{-12}$ to obtain the correct units $ps$).

### 4.3.1 Lifetime Fitting Method

To measure the $\Xi_b^-$ lifetime we used a binned maximum likelihood fit on the reduced proper time. This method is used in low numbers of events and uses Poisson likelihood in each bin.

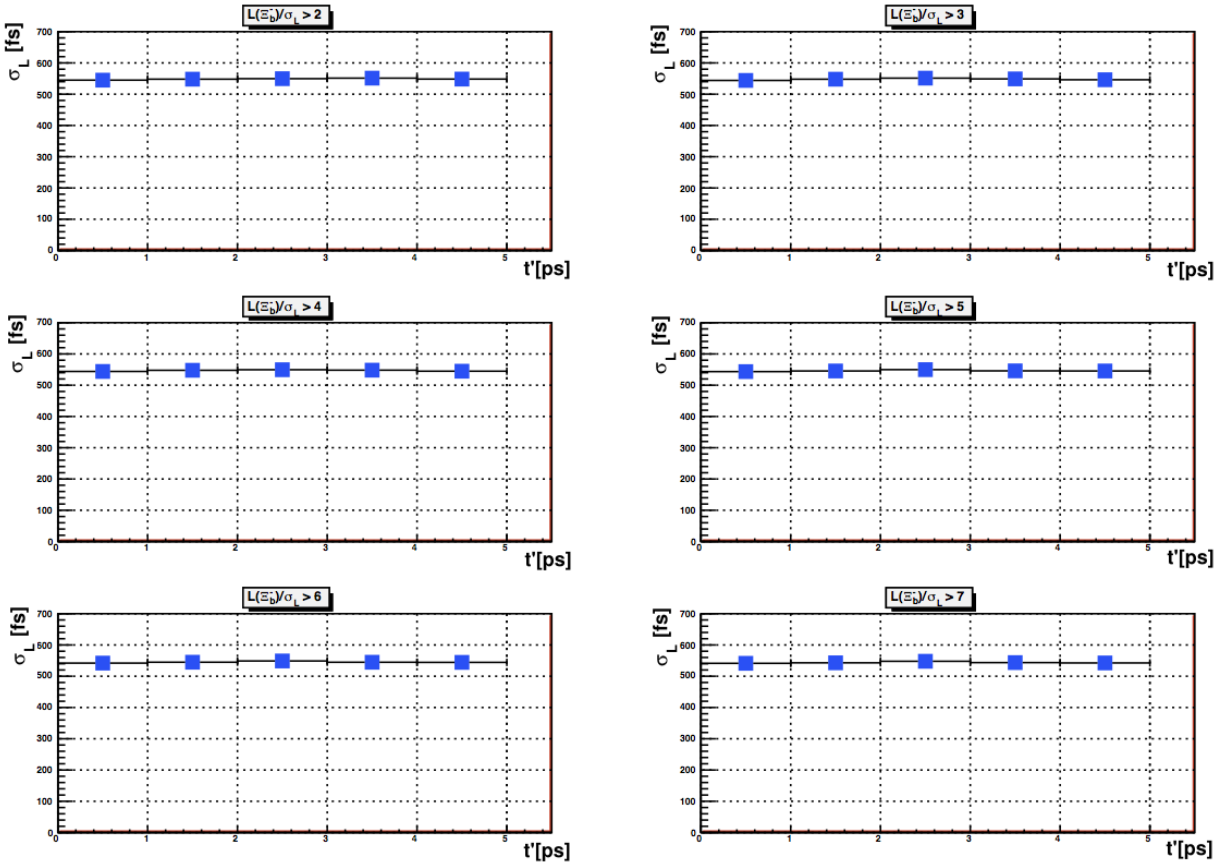


Figure 4–16: $\sigma_L$ mean vs $t'$ for the different $L(\Xi_b^-)/\sigma_L$ cuts.

Furthermore, the reason to use the reduced proper time to find the lifetime is that $t'$ is independent of the resolution. To prove this affirmation we measured the $\sigma_L$ distribution in function of $t'$, (See Figure 4–16). To make these plots we measured the $\sigma_L$ distribution of each picosecond for each $L(\Xi_b^-)/\sigma_L$ cut, then the points in the plot represent the mean value of $\sigma_L$ in the distributions for $0-1\ ps$, $1-2\ ps$, $2-3\ ps$ and $4-5\ ps$. Also, the other cuts for the $\Xi_b^-$ selection (See Table 4–1) were fixed to make these plots.

Figure 4–16 shows a uniform value for $\sigma_L$ with the different $L(\Xi_b^-)/\sigma_L$ cuts vs the reduced proper time $t'$. It implies that $t'$ can be used to measure the lifetime of the baryon since the resolution is independent of it.

Additionally, the reduced proper time is obtained for the $\Xi_b^-$ candidates and the background signal (sidebands). We expected an exponential behaviour in the reduced proper time for the signal region and for the sidebands. The sidebands are composed of background events whereas in the signal region will found signal and background evens. To measure the lifetime it is assumed that the background events in the signal region histogram will have the same behaviour than in the background in the sidebands histograms. Then, to confirm these hypothesis, the background will be taken from two different ways: *i*) from the $\Xi_b^-$ signal, and *ii*) from the $\Xi^-$ signal, as explained below.

**Background taken from the $\Xi^-$ Signal**

Three histograms of the reduced proper time were used from the $\Xi^-$ candidates, one from the signal region with a mass window cut of 0.01 $MeV/c^2$ around the nominal value (1321.7 $MeV/c^2$) and two for the side bands (one left and one right) taken since 0.015 $MeV/c^2$ until 0.025 $MeV/c^2$ away from the nominal value; using the $\Xi_b^-$ region with $3\sigma$ amplitude constant, as is shown in the Figure 4–17.

**Background taken from the $\Xi_b^-$ Signal**

Three histograms of the reduced proper time are used from the $\Xi_b^-$ candidates, one for the signal region with $3\sigma$ amplitude and two for the side bands (one left and one right) taken $5\sigma$ away from the mean value; using the $\Xi^-$ candidates with a mass window cut of 10 $MeV/c^2$, as shown in Figure 4–18.

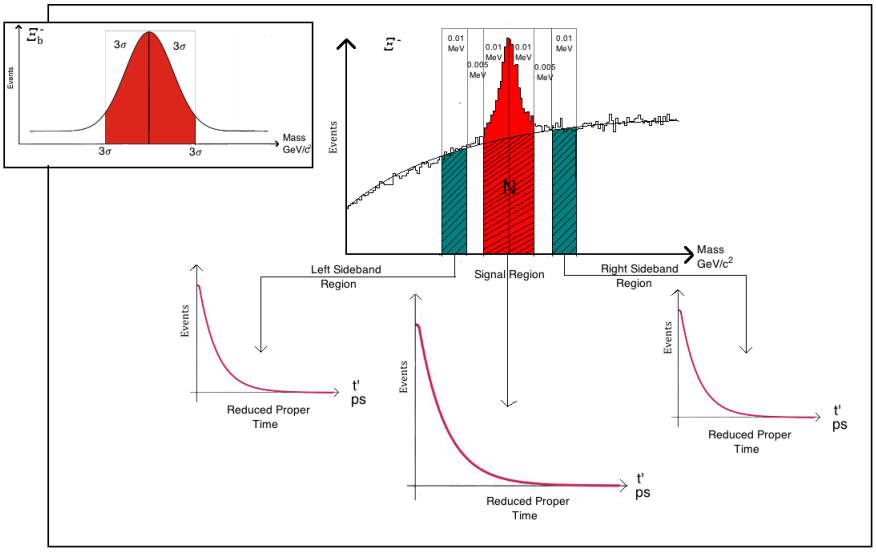


Figure 4–17: Reduced Proper Time Histograms used in the lifetime method with the background taken from the $\Xi^-$ candidates.

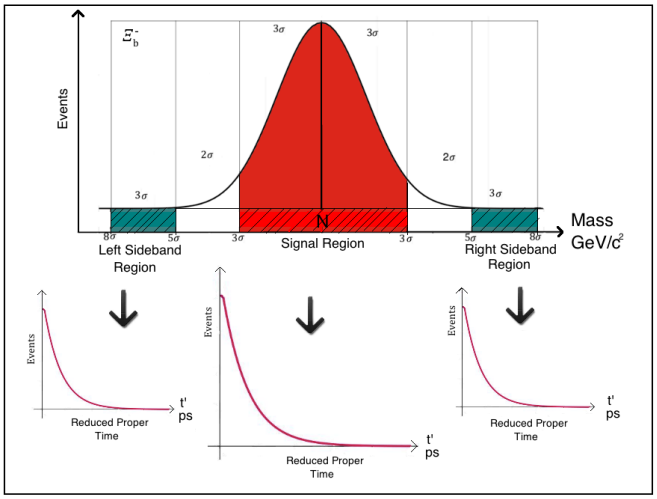


Figure 4–18: Reduced Proper Time Histograms used in the lifetime method with the background taken from the $\Xi_b^-$ candidates.

In addition to what is explained above, the reduced proper time reconstructed may suffer distortions in some stages of the process, for example in some analysis cuts (like $L/\sigma_L$), detector efficiencies, triggering, among others. Then, some studies show these effects in terms of a correction function ($f(t')$), which is determined using Monte Carlo simulations of the experiment and reproducing the sample with the same analysis cuts. Then, the correction function is obtained by dividing the Monte Carlo reduced proper time distribution by the Monte Carlo general lifetime [26].

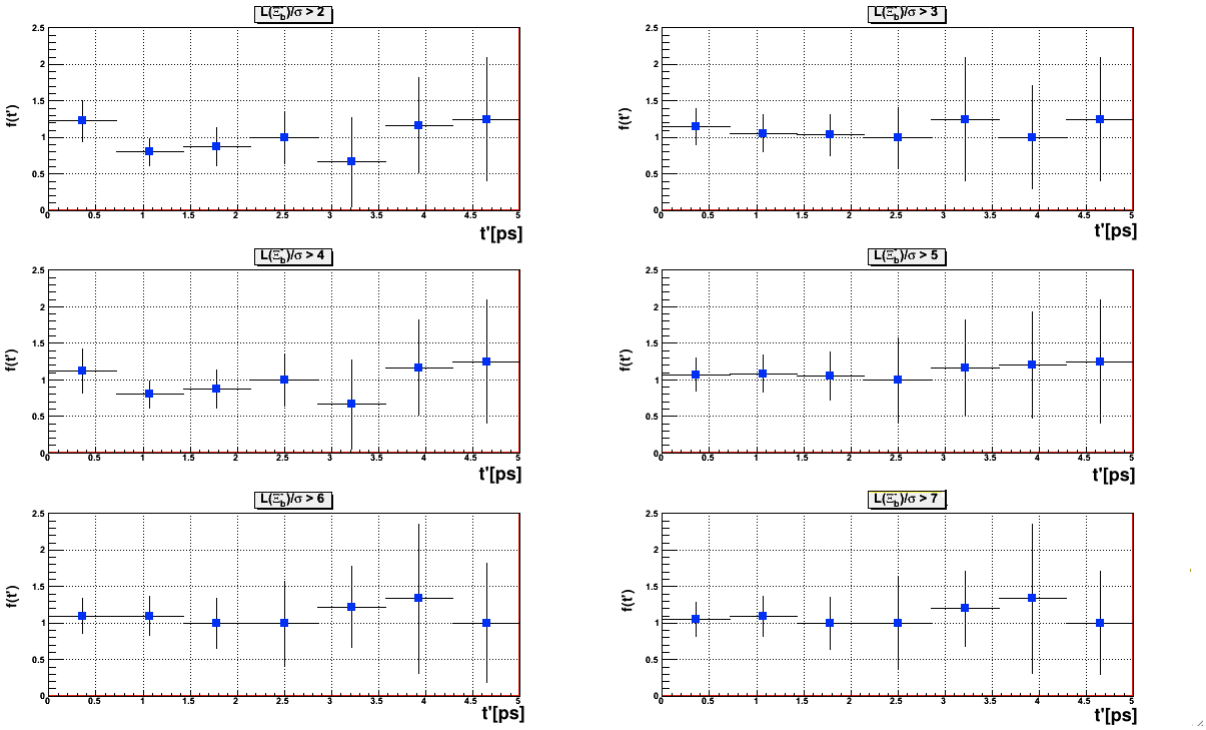


Figure 4–19: Correction function $f(t')$ for the different $L(\Xi_b^-)/\sigma_L$ cuts.

In this preliminary measurement we do not use Monte Carlo simulations; however, we predict that the corrections will be minimal since we constructed a correction function $f(t')$ using the ratio between the reduced proper time of the signal region without triggering and the reduced proper time of the signal region with triggering (specifically, the triggers are shown in the Table 4–3; it means that the reduced proper time was reconstructed before and after pass those tiggers), which is shown in the Figure 4–19.

A constant behaviour for $f(t')$ can be observed, especially when the $L(\Xi_b^-)/\sigma_L$ cut increases. It can be explained since when $L(\Xi_b^-)/\sigma_L$ is lower the two vertices could be overlapping, and when this cut increase the two vertices can be distinguished very well. As a result, in this thesis $f(t')$ will be taken as constant.

Subsequently, in the binned maximum likelihood method, the number of events in a reduced proper time bin is given by:

$$n_i = S\frac{f(t'_i)e^{-t'_i/\tau}}{\sum\limits_i f(t'_i)e^{-t'_i/\tau}} + B\frac{b_i}{\sum\limits_i b_i} \tag{4.4}$$

where $\tau$ is the lifetime of the particle, $t'_i$ is the reduced proper time of each bin, $f(t'_i) = constant$, $b_i$ is the reduced proper time for the sidebands, $S$ is the number of signal events and $B$ is the background events in the signal region (thus $S + B$ is the total number of events in the signal histogram). Then,

$$n_i = S\frac{e^{-t'_i/\tau}}{\sum\limits_i e^{-t'_i/\tau}} + B\frac{b_i}{\sum\limits_i b_i} \tag{4.5}$$

and the likelihood used in this thesis is:

$$\mathscr{L} = \left(\prod_i \frac{n_i^{s_i}e^{-n_i}}{s_i!}\right) \times \left(\frac{(\alpha B)\sum\limits_i b_i e^{-\alpha B}}{\left(\sum\limits_i b_i\right)!}\right) \tag{4.6}$$

where $s_i$ are the events observed, $n_i$ are the events expected and $\alpha$ is the ratio of the total width of the sidebands regions to the signal region (in the $\Xi_b^-$ lifetime measurement $\alpha = 1$). The first term in Equation 4.6 is the product of the Poisson probabilities for each reduced proper time bin in the signal region and the second term is the Poisson probability of observing a total of $\sum\limits_i b_i$ background events when $B$ are expected, where the parameters used for the fit are $\tau$ and $B$.

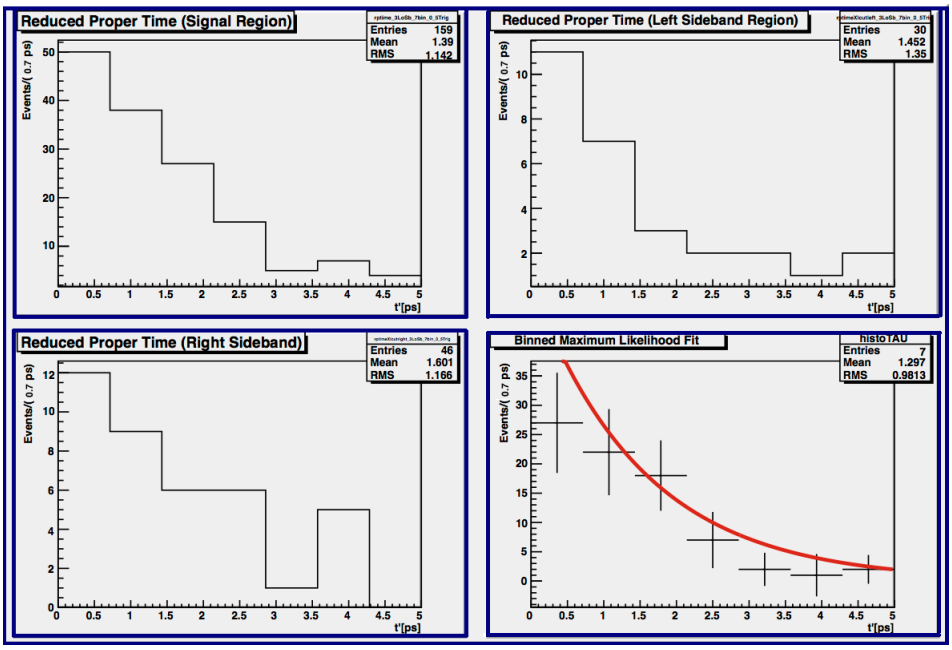


Figure 4–20: Binned Maximum Likelihood Fit on the reduced proper time.

### 4.3.2 Likelihood Method Result

The lifetime was measured using histograms of the reduced proper time with a range from 0 to 5 $ps$, 7 bins and the $L(\Xi_b^-)/\sigma_L > 4$ cut, the fit is shown in the Figure 4–20. As a result of the likelihood method in the reduced proper time of the $\Xi_b^-$ baryon, from 63 events, the lifetime is $\tau = 1.597 \pm^{0.293}_{0.262} ps$.

### 4.3.3 Systematic Uncertainty

Several tests were done in order to verify the measurement. First, the background was taken from two different ways (See Figure 4–17 and Figure 4–18). Second, the $L(\Xi_b^-)/\sigma_L$ cut was varied ($L(\Xi_b^-)/\sigma_L > 2, 3, 4, 5, 6, 7$). And finally, the number of bins was varied in the reduced proper time histograms (5, 7 and 10 bins). The results of these analysis is shown in the Figure 4–21.

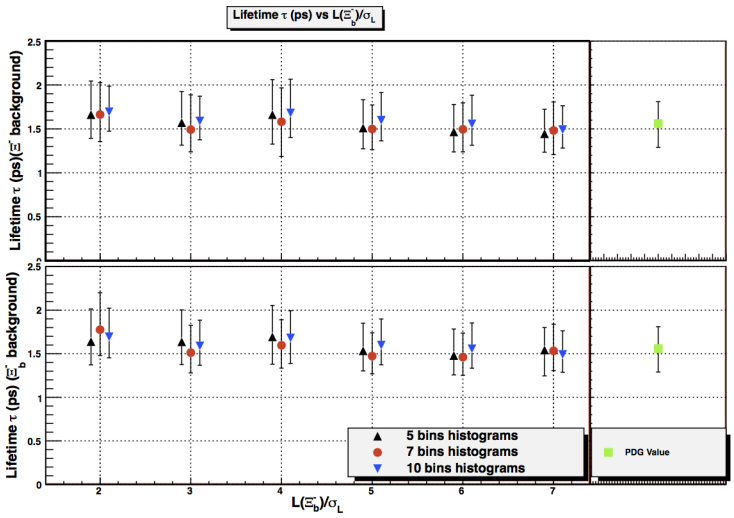


Figure 4–21: Different Lifetime Measurements.

According to the Figure 4–21, the results are stable and to calculate the systematic uncertainty, the number of bins ($t'$ resolution) and the background are used. In addition, to test the method's accuracy, the $\Xi^-$ lifetime was measured as well.

**$t'$ resolution**. The histograms of the reduced proper time were done in a range from 0 to 5 $ps$ and the number of bins used were 5, 7 and 10. Then, the statistical uncertainty due to the $t'$ resolution is the standard deviation of the $L(\Xi_b^-)/\sigma_L > 4$ with 5, 7 and 10 bins ($1.694\pm^{0.360}_{0.314}$ $ps$, $1.597\pm^{0.293}_{0.262}$ $ps$, and $1.681\pm^{0.312}_{0.293}$ $ps$, respectively).

**Background**. Two measurements were done for $L(\Xi_b^-)/\sigma_L > 4$ with different backgrounds. One with the background taken from the $\Xi_b^-$ candidates and other with the background taken from the $\Xi^-$ candidates (See Figure 4–21). Then, the statistical uncertainty due to the background is the standard deviation of these two measurements ($1.597\pm^{0.293}_{0.262}$ $ps$ and $1.581\pm^{0.386}_{0.334}$ $ps$).

**Method's Accuracy**. The $\Xi^-$ lifetime was measured (the results are shown in the Figure 4–22), since this measurement has been done by several experiments [9], it proves

the method's accuracy. As in the $\Xi_b^-$ lifetime measurement, three histograms were taken (one for the signal region and two for the backgrounds).

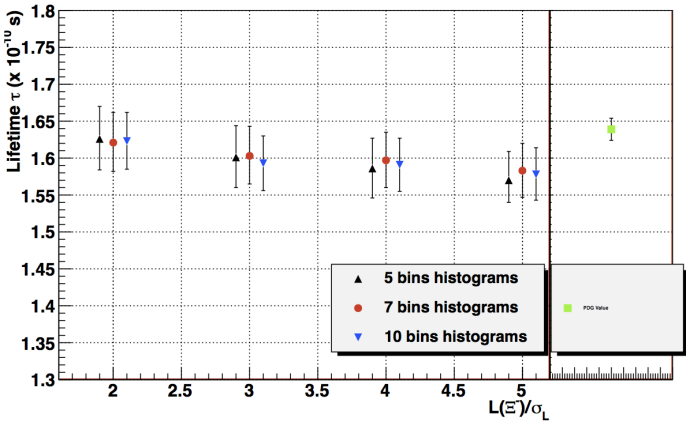


Figure 4–22: $\Xi^-$ Lifetime Measurements.

Figure 4–8 and Figure 4–15 show that the background does not have the same shape for the $\Xi^-$ and the $\Xi_b^-$ masses distributions. Consequently, the $\alpha$ factor is not the same for all the measurements of the $\Xi^-$ lifetime, it corresponds to the ratio of the total width of the sidebands regions to the signal region. A better approach correction would be the function generated by the Monte Carlo Simulation to improve the lifetime measurement. Therefore, we take the systematic uncertainty due to the method's accuracy as the difference between the $\Xi^-$ lifetime given by the PDG value ($(1.639 \pm 0.015) \times 10^{-10}$ $s$) and the value obtained for 7 bin and $L(\Xi^-)/\sigma_L > 4$ cut ($1.597 \pm^{0.038}_{0.037} \times 10^{-10}$ $s$) divided by the nominal value, which represents the 2.5% of the measurement.

The three systematic contributions are added in quadrature in order to obtain the total systematic uncertainty. Table 4–5 summarizes the contributions and the total uncertainty.

Table 4–5: Contribution to the systematic uncertainty.

| Contribution | Uncertainty ($ps$) |
|---|---|
| $t'$ Resolution | $\pm 0.042$ |
| Background | $\pm 0.007$ |
| Method's Accuracy | $\pm 0.042$ |
| Total | $\pm 0.060$ |

Finally, the preliminary $\Xi_b^-$ baryon lifetime with 63 events with a mean mass of $5.798 \pm 0.015\ GeV/c^2$ is $\tau = 1.597\ ^{+0.293}_{-0.262} \pm 0.060\ ps$, where the first error is statistical and the second is systematic.

# CHAPTER 5
# CONCLUSIONS

In this thesis a preliminary measurement of the $\Xi_b^-$ lifetime was done through the decay chain $\Xi_b^- \to J/\psi\Xi^-$, where $J/\psi \to \mu^+\mu^-$, $\Xi^- \to \Lambda^0\pi^-$ and $\Lambda^0 \to p\pi^-$, using 5.1 $fb^{-1}$ of integrated luminosity of data from $pp$ collisions at 7 $TeV$ collected by CMS at CERN.

The decay channel was reconstructed using the selection cuts of Table 4–1 and to measure the lifetime of the baryon a $L(\Xi_b^-)/\sigma_L > 4$ cut was used, where $L(\Xi_b^-)/\sigma_L$ represents the vertex separation significance. As a result of this process, 63 events were reconstructed with a mean mass of $5.797 \pm 0.015\ GeV/c^2$ ( $5.7911 \pm 0.022\ GeV/c^2$ is the nominal Value); where the $\Xi_b^-$ mass background could be from the $\Omega^-$ particles which can decay into $K^-\Lambda^0$ or $\Xi^-\pi^0$.

Next, the binned maximum likelihood fit on the reduced proper time of the data reconstructed was done. Here, the reduced proper time was used because this variable is independent of the resolution of the reconstruction (as is shown the Figure 4–16). Also, the correction function was taken as constant (See Figure 4–19) where the correction function is the ratio between the reduced proper time of the signal region without triggering and the reduced proper time of the signal region with triggering.

Furthermore, the binned maximum likelihood fit used three histograms, one for the signal region and two for the background taken from the sidebands. In the signal region, it is expected to have signal events and background events. The background events from the signal region have a similar behaviour as the background taken from the sidebands.

Several measurements were done (See Figure 4–21) in order to check this measurement using different resolution, $L(\Xi_b^-)/\sigma_l$ cut and taken the background of two

ways, one from the $\Xi^-$ candidates (See Figure 4–17) and other from the $\Xi_b^-$ candidates (See Figure 4–18). In addition, to test the method's accuracy the $\Xi^-$ lifetime was measured, this measurement was well done in other experiments (The nominal value is $(1.639 \pm 0.015) \times 10^{-10} s$). As a result, the systematic uncertainties were added in quadrature to obtain the uncertainty of the measurement and a better correction function to improve the lifetime method precision will be needed.

Finally, the lifetime $\tau = 1.597 \pm^{0.293}_{0.262} \pm 0.060\ ps$ was measured, where the first error is statistical and the second is systematic.

## 5.1 Previous Measurements

The PDG has only one measure of the $\Xi_b^-$ lifetime up to now and it corresponds to the nominal value. They measured a mass of $5.7909 \pm 0.0026(stat.) \pm 0.0008(syst.)$ $GeV/c^2$, 66 events and a lifetime of $1.56 \pm^{0.27}_{0.25} (stat.) \pm 0.02(syst.)$ $ps$ for the $\Xi_b^-$ particle, using 4.2 $fb^{-1}$ of data from $p\overline{p}$ collisions at a center-of-mass of 1.96 $TeV$ from data recorded with the Collider Detector at Fermilab (CDF), in the same decay channel $(\Xi_b^- \to J/\psi \Xi^-)$ [28].

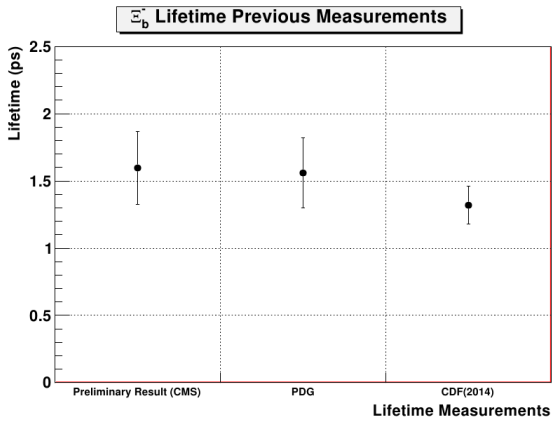


Figure 5–1: Previous $\Xi_b^-$ lifetime measurements.

Furthermore, on March 31, 2014, the CDF collaboration published a measure of $5.7934 \pm 0.00031(stat.) \pm 0.00047(syst.)$ $GeV/c^2$, 112 events and a lifetime of $1.32 \pm$

$0.14(stat.) \pm 0.02(syst.)\ ps$ for the $\Xi_b^-$ particle, using 9.6 $fb^{-1}$ of data from $p\overline{p}$ collisions at a center-of-mass of 1.96 $TeV$ from data recorded with the CDF, in the same decay channel [29].

Therefore our previous lifetime measurement agrees with the nominal value. However, it is expected that using Monte Carlo Simulations and with the 2012 Data Sample from CMS at a center-of-mass of 8 $TeV$ (higher luminosity), the $\Xi_b^-$ lifetime measurement will improve.

## 5.2 Future Work

Given the good preliminary results of the lifetime of the $\Xi_b^-$ baryon, we propose:

- Use the 2012 Data Sample of CMS to repeat the measurement, then the statistical data will be larger and it is expected than the statistical uncertainty of the measurement will decrease.
- Implement algorithms which allow to clean the $\Xi_b^-$ mass signal of possible contamination from $\Omega^-$ particles.
- Using the new data, it is possible to use less restrictive cuts in the mass windows of $\Lambda^0$ and $\mu^+\mu^-$ candidates, to prove the accuracy of the constraints.
- Use Monte Carlo simulations of the $\Xi_b^- \rightarrow J/\psi\Xi^-$ decay channel to improve the correction function and hence the lifetime measurement.

# APPENDICES

# APPENDIX A
# VETO MASS WINDOW OF THE $\Lambda^0$ CANDIDATES

To show the validity of the veto mass window cut used with the $\Lambda^0$ candidates, Figure A–1 shows a scattering plot between the $\Lambda^0$ and the $\Xi^-$ candidates mass which evidences the mass distribution of these particles.

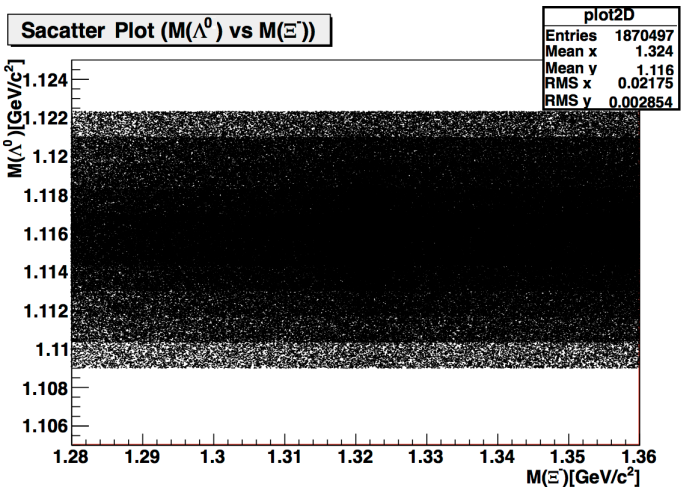


Figure A–1: Scattering plot between the $\Lambda^0$ and the $\Xi^-$ candidates mass.

To study the possible $\Xi_b^-$ particles rejected with the mass window cut chosen for the $\Lambda^0$ candidates (6 $MeV$), the $\Xi_b^-$ will be reconstructed with different mass windows cuts in the signal of the $\Lambda^0$ and the $\Xi^-$ candidates mass which are shown in Figure A–2. The mass window cut chosen for the $\Lambda^0$ candidates is $S_1$, and it represents the $\Xi^-$ candidates shown in Figure A–2-b. Furthermore, the signal of the $\Xi^-$ candidates lost for reject $\Lambda^0$ candidates with a mass taken since 6 $MeV$ until 9 $MeV$ away from the nominal value is shown in Figure A–2-c.

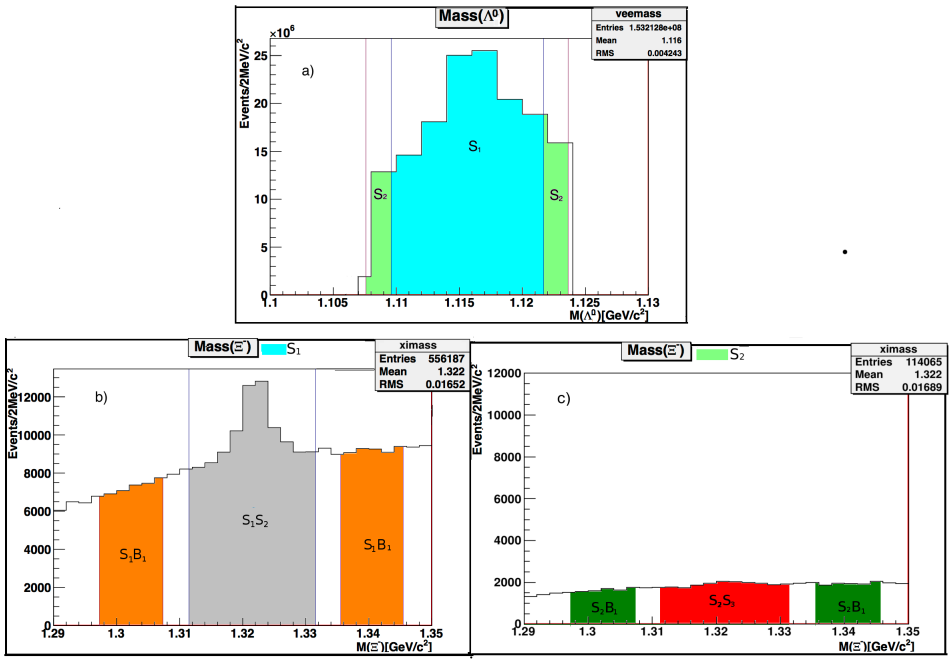


Figure A–2: Windows mass cuts in the a) $\Lambda^0$, b) $\Xi^-$ signal from the $S_1$ region of the $\Lambda^0$ candidates and c) $\Xi^-$ signal from the $S_2$ region of the $\Lambda^0$ candidates (These are the $\Xi^-$ rejected.)

In addition, it is not possible to take signal farther away from the nominal value of the $\Lambda^0$ candidates because in the reconstruction process of the $\Xi^-$ candidates, we cut the $\Lambda^0$ candidates with a mass 10 $MeV$ away from the nominal value. Also, the other cuts in the selection process are the same as those shown in Table 4–1.

Figure A–3 shows the $\Xi_b^-$ signal obtained for the different cuts of the $\Lambda^0$ and $\Xi^-$ masses. Figure A–3-a is the final signal while the other are the background which was removed. Also, Figure A–3-d shows the specific events rejected doing the window mass cut of the $\Lambda^0$ of 6 $MeV$ and not of 9 $MeV$. It is shown that only background events were rejected.

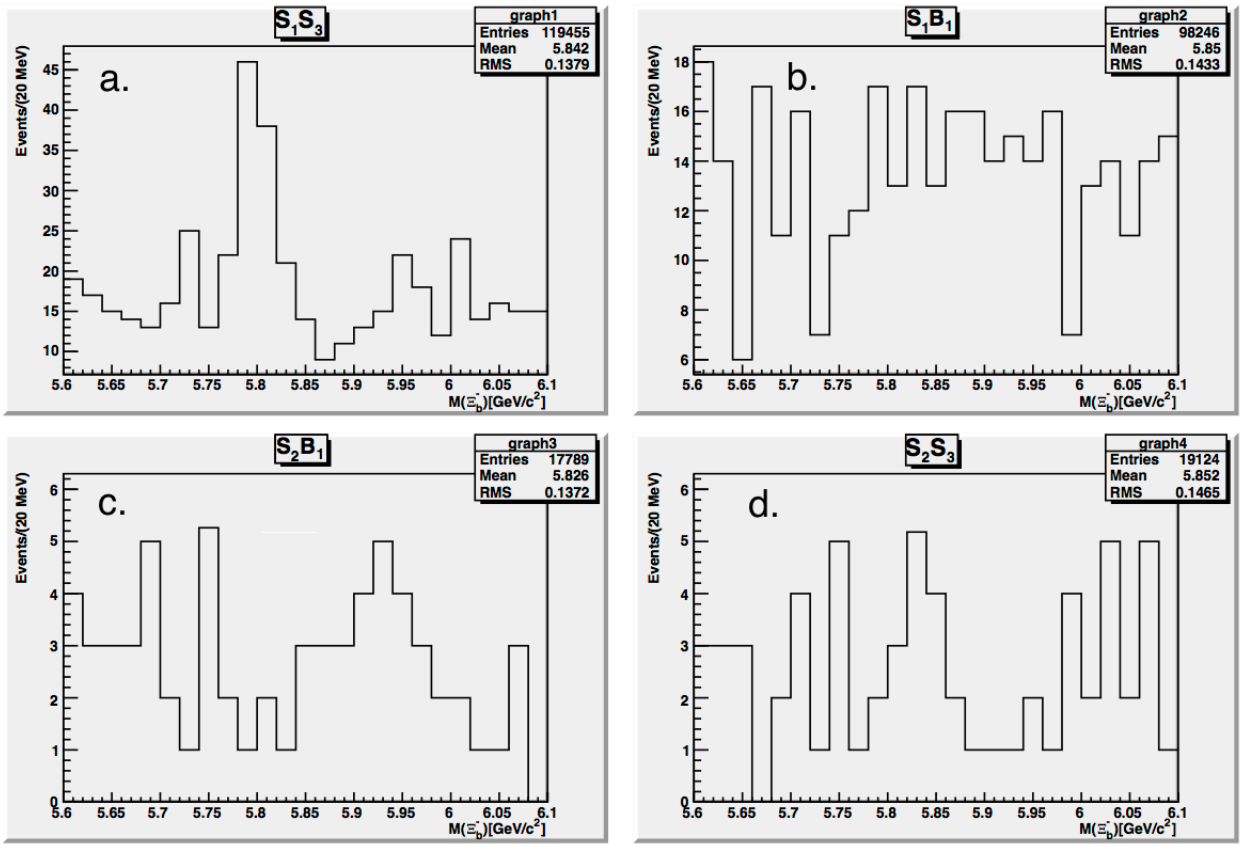


Figure A–3: Different windows cut in the $\Lambda^0$ and $\Xi^-$ masses.
a) $S_1$ and $S_3$ cuts, b) $S_1$ and $B_1$ cuts, c) $S_2$ and $B_1$ cuts and d) $S_2$ and $S_3$ cuts.

# APPENDIX B
# VETO MASS WINDOW OF THE $\mu^+\mu^-$ CANDIDATES

To show the validity of the veto mass window cut used with the $\mu^+\mu^-$ candidates, Figure B–1 shows a scattering plot between the $\mu^+\mu^-$ and the $\Xi^-$ candidates mass which evidences the mass distribution of these particles.

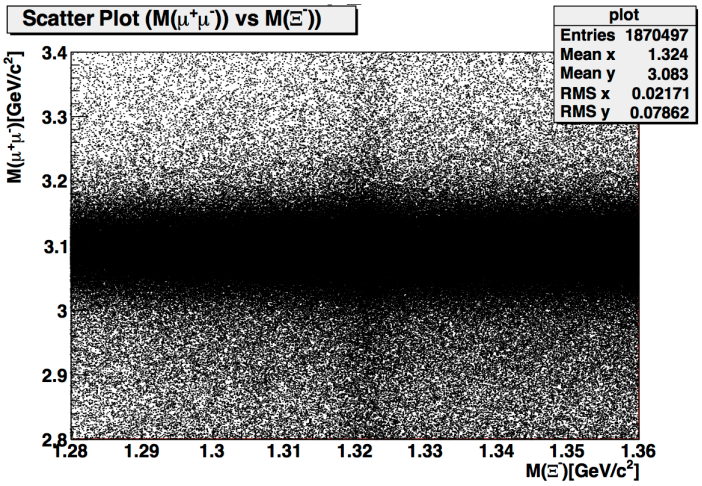


Figure B–1: Scattering plot between the $\mu^+\mu^-$ and the $\Xi^-$ candidates mass.

To study the possible $\Xi_b^-$ particles rejected with the mass window cut chosen for the $\mu^+\mu^-$ candidates (50 $MeV$), the $\Xi_b^-$ will be reconstructed with different mass windows cuts in the signal of the $\mu^+\mu^-$ and the $\Xi^-$ candidates mass which are shown in Figure B–2. The mass windows cuts chosen for the $\mu^+\mu^-$ and $\Xi^-$ candidates are $S_1$ and $S_2$ respectively. Furthermore, the signal for the $\mu^+\mu^-$ mass candidates is taken since 50 $MeV$ until 150 $MeV$ away from the nominal value ($S_2$) and background events ($B_1$). Also, in the signal of the $\Xi^-$ candidates is taken background events ($B_2$).

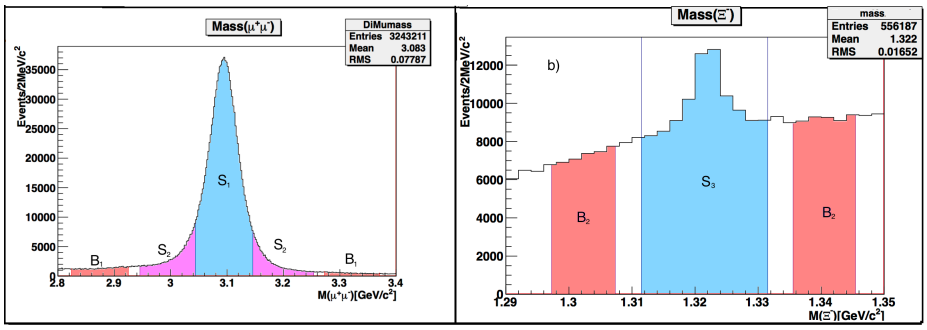


Figure B–2: Windows mass cuts in the a)$\Lambda^0$ and b) $\Xi^-$ signals.

In addition, the other cuts in the selection process are the same as those shown in Table 4–1.

Figure B–3 shows the $\Xi_b^-$ signal obtained for the different cuts of the $\mu^+\mu^-$ and $\Xi^-$ masses. Figure B–3-a is the final signal while the other are the background which was removed. Also, Figure A–3-f shows the specific events rejected doing the window mass cut of the $\mu^+\mu^-$ of 50 $MeV$ and not of 150 $MeV$. It is shown that only background events were rejected.

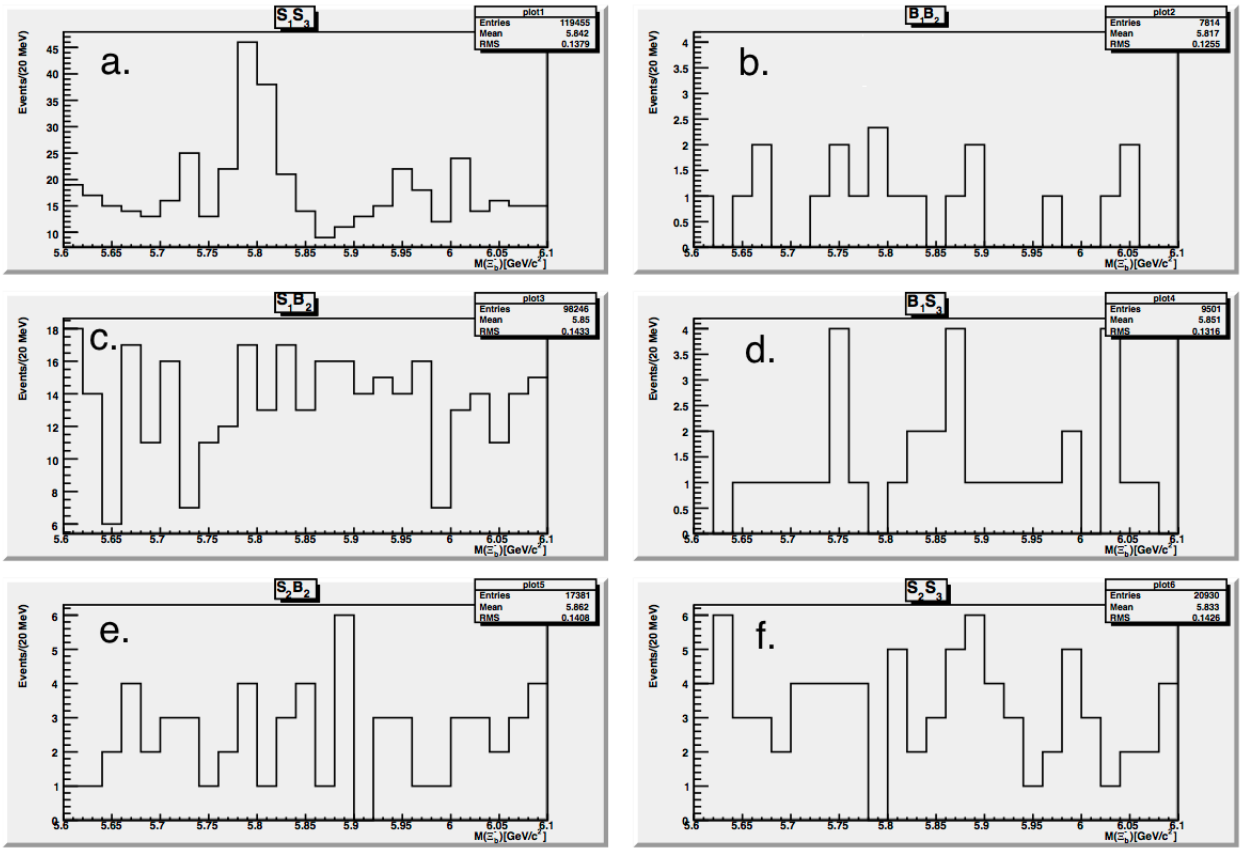


Figure B–3: Different windows cut in the $\mu^+\mu^-$ and $\Xi^-$ masses.
a) $S_1$ and $S_3$ cuts, b) $B_1$ and $B_2$ cuts, c) $S_1$ and $B_2$ cuts, d) $B_1$ and $S_3$ cuts, e) $S_2$ and $B_2$ cuts and $S_2$ and $S_3$.

# APPENDIX C
# DATASETS

This appendix contains the paths of the Datasets used in the analysis. The datasets taken from the 2011 sample are:

- */MuOnia/Run2011A-May10ReReco-v1/AOD*,
- */MuOnia/Run2011A-05Aug2011-v1/AOD*,
- */MuOnia/Run2011A-PromptReco-v4,v6/AOD*,
- */MuOnia/Run2011B-PromptReco-v1/AOD*.

The JSON file used is:

- *Cert_160404-180252_7TeV_PromptReco_Collisions11_JSON_MuonPhys.txt*

REFERENCES


[1] L. Hoddeson. *The Rise of the Standard Model: A History of Particle Physics from 1964 to 1979*. Cambridge University Press, first edition, 1997.

[2] W.N. Cottingham and D. A. Greenwood. *An Introduction to the Standard Model of Particle Physics*. Cambridge University Press, second edition, 2007.

[3] Scientific Explorer. *Supersymmetry*. http://sciexplorer.blogspot.com/2013/10/supersymmetry.html, 2013.

[4] Wei et al Chao. *Higgs Vacuum Stability, Neutrino Mass, and Dark Matter*. *Phys.Rev.*, D86, 2012. iop:10.1103/PhysRevD.86.113017.

[5] F. Halzen and A. Martin. *QUARKS AND LEPTONS: An Introductory Course in Modern Particle Physics*. John Wiley and Sons. Inc, first edition, 1984.

[6] D. Griffiths. *Introduction to Elementary Particles*. John Wiley and Sons. Inc, first edition, 1987.

[7] E-ducation. *M-theory*. http://e-ducation.net/physics.htm, 2013.

[8] CMS Collaboration. *Observation of a new boson with mass near 125 GeV in pp collisions at* $\sqrt{s}$ *7 and 8 TeV*, 2013 j. phys.: Conf. ser. 447 012010, doi:10.1088/1742-6596/447/1/012010. *[arxiv:1303.4571v1]*.

[9] J. Beringer et al. (Particle Data Group). *The Review of Particle Physicss*. Phys. Rev., d86, 010001 edition, 2012.

[10] et al V. Abazov. *Direct Observation of the Strange b Baryon* $\Xi_b^-$. *Phys. Rev. Lett.*, **99**(5), 2007. DOI:10.1103/PhysRevLett.99.052001.

[11] H. Murayama. *Physics Beyond the Standard Model and Dark Matter*. Les Houches Summer School, Session 86. Particle Physics and Cosmology: the Fabric of Space-time. July 31- August 25 (2006). arXiv:0704.2276.

[12] C. Scholz B. Povh, K. Rith and F. Zetsche. *Particles and Nuclei. An Introduction to the Physical Concept*. Springer, sixth edition, 2008.

[13] F.Soler M. Kramer. *LARGE HADRON COLLIDER PHENOMENOLOGY*. Scottish Universities Summer School in Physics and Institute of Physics Publishing, Bristol and Philadelphia, 2004.

[14] Cern: public web. "*Cern Complex*", 2012. [Online; accessed 2-July-2013] http://home.web.cern.ch/about/accelerators.

[15] CMS Collaboration. *Compact Muon Solendoid (CMS)*. (27 Jun 2013, StoyanStoynev) http://cms.web.cern.ch/content/cms-collaboration.

[16] Cern: public web. *CMS detector design*, note = https://http://cms.web.cern.ch/news/cms-detector-design .

[17] CMS Collaborationl. *The CMS experiment at the CERN LHC*. *JINST*, **3**, 2007. doi:10.1088/1748-0221/3/08/S08004.

[18] The Particle Adventure. *Detector cross section*. http://www.particleadventure.org.

[19] C. Favaro. *Study of the Associated Production of a Z Boson with b Hadrons in Proton-Proton Collisions with the CMS Experiment*. Dissertation, Universiry of Zurich, 2013.

[20] T. Ferbel. *Experimental Tchniques in High Energy Physics*. Addison-Wesley Publishing Company, Inc, 1987.

[21] CMS Collaboration. *Technical Proposal for the Upgrade of the CMS detector through 2020*. Technical Report CERN-LHCC-2011-006. LHCC-P-004, CERN, Geneva, Jun 2011.

[22] C. Larrea J. Hammer C. Hartl C. Lazaridis M. Magrans de Abril M, J. Da Rocha Melo. *The architecture of the CMS Level-1 Trigger Control and Monitoring System using UML*. 2011 J. Phys.: Conf. Ser. 331 022020, doi:1742-6596/331/2/022020.

[23] CERN Courier. *Pulling the trigger on LHC electronics*. Jan 25, 2001 http://cerncourier.com/cws/article/cern/28367/2.

[24] CMS Collaboration. *CMS TriDAS project: Technical Design Report, Volume 2: Data acquisition and high-level trigger technical design repor.* Technical Report CERN-LHCC-2002-026, CERN, Geneva, 2002.

[25] A. Rafique. *Measurement of Muon Performance and Determination of Z Boson Production Cross Section using CMS Detector at LHC.* Dissertation, QUAID-I-AZAM UNIVERSITY, ISLAMABAD, June 2013.

[26] J. E. Ramirez. *Lifetime Measurement of the Charmed Strange BAryon* $\Xi_c^+$. Dissertation, QUAID-I-AZAM UNIVERSITY, ISLAMABAD, University of Colorado.

[27] CMS Collaboration. *The TAUFIT lifetime fitting program.* Technical Report Ref:WA89 96.08, L. Schmitt and S. Masciocchi, WA89 Collaboration, Jun 1997.

[28] T. Aaltonen et al. *Observation of the* $\Omega_b^-$ *Baryon and Measurement of the Properties of the* $\Xi_b^-$ *and* $\Omega_b^-$ *Baryons.* *Phys.Rev.*, D80:072003, 2009. doi:10.1088/1748-0221/3/08/S08004.

[29] T. Aaltonen et al. *Mass and lifetime measurements of bottom and charm baryons in* $p\overline{p}$ *collisions at* $\sqrt{s} = 1.96\ TeV$. *Phys.Rev.*, D89:072014, 2014. doi:10.1103/PhysRevD.89.072014.